This is a preprint, the final version is subject to change, of the American Mineralogist (MSA)
Cite as Authors (Year) Title. American Mineralogist, in press.
(DOI will not work until issue is live.) DOI: http://dx.doi.org/10.2138/am-2017-6115

Revision 1

Experimental and thermodynamic investigations on the stability of $Mg_{14}Si_5O_{24}$ anhydrous phase B with relevance to Mg_2SiO_4 forsterite, wadsleyite and ringwoodite

Hiroshi Kojitani*, Saki Terata, Maki Ohsawa, Daisuke Mori, Yoshiyuki Inaguma, Masaki Akaogi

1-5-1 Mejiro, Toshima-ku, Tokyo 171–8588, Japan

Department of Chemistry, Faculty of Science, Gakushuin University

*Corresponding author: hiroshi.kojitani@gakushuin.ac.jp

Abstract

High-pressure high-temperature phase relation experiments in $Mg_{14}Si_5O_{24}$ were performed using a 6-8 multi-anvil high-pressure apparatus in the pressure range of 12–

22 GPa and temperature range of 1673–2173 K. We first found that $Mg_{14}Si_5O_{24}$ anhydrous phase B (Anh-B) dissociates to Mg_2SiO_4 wadsleysite (Wd) and MgO periclase (Per) at about 18 GPa and 1873 K. From the results of the high-pressure experiments, the phase boundaries of 5 Mg_2SiO_4 forsterite (Fo) + 4 Per = Anh-B and Anh-B = 5 Wd + 4 Per were determined. In addition, the isobaric heat capacity (C_P) of Anh-B was measured by differential scanning calorimetry in the temperature range of 300–770 K and the thermal relaxation method using a Physical Property Measurement System (PPMS) in the range of 2–303 K. From the measured low-temperature C_P, the standard entropy ($S^o_{298.15}$) of Anh-B was determined to be 544.4(2) J/mol·K. We also performed high-temperature X-ray diffraction measurements in the range 303–773 K to determine the thermal expansivity (α) of Anh-B. The obtained C_P and α were theoretically extrapolated to higher temperature region using a lattice vibrational model calculation partly based on Raman spectroscopic data. Thermodynamic calculations by adopting the thermochemical and thermoelastic data for Anh-B obtained in this study and the estimated formation enthalpy for Anh-B of –13208 kJ/mol·K gave phase equilibrium boundaries for 5 Fo + 4 Per = Anh-B and Anh-B = 5 Wd + 4 Per that were consistent with those determined by the present high-pressure high-temperature experiments. The results clarified that, in the $Mg_{14}Si_5O_{24}$ system, Anh-B is stable

37 between 12 and 18 GPa at the expected temperatures of the Earth's mantle.

38

39 Keywords: anhydrous phase B, phase boundary, heat capacity, entropy, thermal
40 expansivity, Raman spectrum, wadsleyite, ringwoodite

41

This is a preprint, the final version is subject to change, of the American Mineralogist (MSA)
Cite as Authors (Year) Title. American Mineralogist, in press.
(DOI will not work until issue is live.) DOI: http://dx.doi.org/10.2138/am-2017-6115

Introduction

A high-pressure dense magnesium silicate $Mg_{14}Si_5O_{24}$ anhydrous phase B (Anh-B) was first synthesized by Herzberg and Gasparik (1989) and its crystal structure was determined by Finger et al. (1989, 1991). The crystal structure contains two different stacking layers. One is a forsterite-like layer consisting of MgO_6 octahedra and SiO_4 tetrahedra, and the other is a layer consisting of MgO_6 and SiO_6 octahedra. The structure is closely related to that of hydrous $Mg_{12}Si_4O_{19}(OH)_2$ phase B, as the name indicates (Finger et al. 1989; 1991). Due to the SiO_6 octahedra, Anh-B has a density higher than that of 5 Mg_2SiO_4 forsterite (Fo) + 4 MgO periclase (Per). Ganguly and Frost (2006) investigated the phase boundary between 5 Fo + 4 Per and Anh-B by using high-pressure high-temperature experiments and thermodynamic calculation. Moreover, by examining the phase stability field of Anh-B + 2 SiO_2 stishovite (St) in the $Mg_{14}Si_7O_{28}$ system using a thermodynamic calculation, they suggested the possibility of the existence of Anh-B in cold subducted oceanic plates around 15 GPa and 800 K.

Crichton et al. (1999) determined an equation of state (EoS) of Anh-B by high-pressure in situ X-ray diffraction (XRD) measurement at room temperature and proposed a bulk modulus and its pressure derivative of 151.5 GPa and 5.5, respectively.

On the other hand, there have been no other experimentally determined thermoelastic data, such as the temperature derivative of the bulk modulus and thermal expansivity, and no thermochemical data on ehthalpy, heat capacity or entropy. Ottonello et al. (2010) made a calculation of the phase equilibrium boundary for 5 Fo + 4 Per = Anh-B using the thermodynamic parameters of Anh-B predicted by *ab initio* calculation and gave a phase boundary very similar to that obtained in Ganguly and Frost (2006).

It has also been observed by Presnall and Gasparik (1990) that, in a high-pressure high-temperature run at 16.5 GPa and 2623 K, Anh-B coexists with liquid on the incongruent melting process of Fo. This fact suggests that around 15 GPa Anh-B may be stable at not only low temperature of about 800 K as described above but also high temperature over 2500 K.

Recently, Bindi et al. (2016) reported that Cr-bearing Anh-B appeared as a high-pressure stability phase in the Mg_2SiO_4–$MgCr_2O_4$ system at 12 GPa and 1873 K. The Mg_2SiO_4–$MgCr_2O_4$ system can be a simplified model for podiform chromitites consisting of chromites surrounded by peridotites such as dunite and harzburgite, which are found in ophiolites and are probably formed by reactions between peridotite and melt (Arai 1997; Arai and Miura 2016). Since ultrahigh-pressure (UHP) minerals of coesite and diamond have been found in the podiform chromitites, it is interpreted that

78 the UHP chromitites may have undergone deep mantle recycling (e.g., Yamamoto et al.
79 2009). Therefore, if Anh-B is discovered in the UHP podiform chromitites, its existence
80 could be a good geobarometer for constraining the origin of the chromitites.

81 It is important to clarify the thermodynamic stability of Anh-B in order to properly
82 interpret the melting relation of Fo at high pressure and high temperature and the origin
83 of the UHP chromitites. However, the detailed phase stability field of Anh-B in a *P–T*
84 space, especially at an upper limit in pressure, is still unknown. In this study, we
85 performed high-pressure and high-temperature experiments in the $Mg_{14}Si_5O_{24}$ system
86 up to 22 GPa and 2073 K to experimentally determine the high-pressure phase relations.
87 In addition, the stability field of Anh-B was also examined by a thermodynamic
88 approach. Thermal expansivity of Anh-B was determined by high-temperature X-ray
89 diffraction (XRD) measurement, and the low- and high-temperature heat capacities of
90 Anh-B were measured using a Physical Property Measurement System (PPMS) and a
91 differential scanning calorimeter (DSC), respectively. From the measured
92 low-temperature heat capacity, the standard entropy of Anh-B was also obtained. The
93 measured heat capacity and thermal expansivity were extrapolated to a higher
94 temperature region using a lattice vibrational model calculation partly based on the
95 Raman spectrum observed in this study. The thermodynamic data thus obtained were

applied to estimation of the stability field of Anh-B in the ranges of 10–21 GPa and 300–2700 K by a thermodynamic approach.

Experimental methods

High-pressure high-temperature experiments and sample characterization

Starting materials of high-pressure high-temperature experiments on anhydrous phase B were synthesized as follows. Mg_2SiO_4 Fo was prepared from a mixture of analytical grade reagents of MgO Per and SiO_2 quartz with a 2:1 mole ratio by heating at 1773 K for 56 h, and it was confirmed to be a single-phase by the powder XRD method. An intimate mixture of Fo and Per with a mole ratio of 5:4 was used as the starting material for most of the high-pressure high-temperature experiments. $Mg_{14}Si_5O_{24}$ Anh-B and a mixture of Mg_2SiO_4 wadsleyite (Wd):Per = 5:4 in mole ratio were used as the starting materials for reverse runs. The Anh-B sample for the reverse run was synthesized from the mixture of Fo and Per with a mole ratio of 5:4 at 15 GPa and 1873 K for 3 h, and Wd was prepared by holding Fo at 16 GPa and 1873 K for 2 h.

114 High-pressure high-temperature experiments were performed at 12–23 GPa and
115 1673–2073 K using a Kawai-type 6–8 multi-anvil apparatus at Gakushuin University.
116 Tungsten carbide anvils with a truncated edge length (TEL) of 2.5 and 5.0 mm were
117 used in combination with a semi-sintered 5 wt% Cr_2O_3-doped MgO octahedron of 7 and
118 10 mm-edge, respectively, as the pressure media. Pressure calibration was made at room
119 temperature using pressure-fixed points of Bi I–II (2.55 GPa), Bi III–V (7.7 GPa), ZnS
120 (15.5 GPa), GaAs (18.3 GPa) and GaP (23 GPa) (Dunn and Bundy, 1978; Ito, 2007).
121 The pressure was corrected at 1873 K using coesite–stishovite transition in SiO_2 (Zhang
122 et al., 1996), forsterite–wadsleyite transition (Morishima et al. 1994) and wadsleyite–
123 ringwoodite transition (Inoue et al. 2006) in Mg_2SiO_4, and akimotoite–bridgmanite
124 transition in $MgSiO_3$ (Ono et al. 2001). The pressure calibration was also made at 1673
125 K and 2073 K in a similar manner to that at 1873 K. The uncertainties in the generated
126 pressures and temperature in the present experiments were estimated to be less than
127 about ±0.3 GPa and ±20 K, respectively. In the high-pressure phase relation
128 experiments, a tubular rhenium heater was placed in the central part of the pressure
129 medium of magnesia octahedron. A $LaCrO_3$ sleeve and end-plugs were inserted between
130 the Re heater and the pressure medium for thermal insulation. The starting materials
131 were placed directly in the Re furnace, and kept at desired pressure and temperature

conditions for 1–3 h, then quenched, and returned to ambient conditions. The run temperature was measured at the central part of the outer surface of the Re heater by a Pt/Pt–13%Rh thermocouple. The pressure effect on emf of the thermocouple was ignored.

The recovered samples were examined by microfocus and powder X-ray diffractometers (RINT 2500V; Rigaku). Cr Kα radiation with a rotating anode was used at 45 kV and 250 mA for both the XRD measurements. For the microfocus XRD measurement, a collimated X-ray beam of 50 μm diameter was used. Lattice parameters of anhydrous phase B were determined by using a powder X-ray diffractometer with the step-scan method at 0.02° step.

A part of the run product of anhydrous phase B was mounted on a slide glass plate with epoxy resin, and polished for compositional analysis by a scanning electron microscope (SEM) (JMS-6360; JEOL) with the energy dispersive X-ray spectrometer (EDS) (Sirius SD 10133BE-IS; SGX Sensortech). The SEM was operated with an acceleration voltage of 15 kV and probe current of 0.55 nA. The composition analysis was made at 12 analysis points. Standard material for Mg and Si was a synthetic $MgSiO_3$ orthoenstatite.

Anh-B samples for the PPMS measurement were also synthesized with the

Kawai-type multianvil apparatus using the second stage tungsten carbide anvils with TEL of 5.0 mm. The pressure medium was the 5 wt% Cr_2O_3-doped MgO octahedron with 10 mm edge. The $LaCrO_3$ sleeve was used as a heater. Inside the $LaCrO_3$ sleeve, two Pt capsules containing the starting sample were placed symmetrically. The Pt capsules were surrounded by MgO sleeves in order to electrically insulate them from the $LaCrO_3$ heater. The temperature was monitored by a W5%–Re95%/W26%–Re74% thermocouple whose hot junction was placed at the center between the two Pt capsules. The starting sample of the mixture of Fo:Per = 5:4 in mole ratio was kept at 15 GPa and 2073–2273 K for 3 h and then quenched by turning off the electric power and decompressed to ambient pressure. Composition analysis indicated that the synthesized sample consisted of MgO of 66.18(33) wt% and SiO_2 of 34.41(40) wt% with total 100.59(60) wt%, resulting in an Mg:Si atomic ratio of 14.1(1):4.9(1) on a 24-oxygen basis from the average of 12 data points, where the numerals in parentheses represent twice the standard deviation of the mean.

High-temperature X-ray diffraction measurement

To measure the thermal expansion of Anh-B, high-temperature XRD experiments

were carried out using a powder X-ray diffractometer (RINT 2100; Rigaku) with a high-temperature cell. The diffractometer with CuKα radiation was operated at 40 kV and 40 mA in the 2θ range of 10–70° with steps of 0.02°. High-purity Si was used as the internal 2θ standard. The sample temperature was monitored with a Pt/Pt–13%Rh thermocouple. Before the high-temperature XRD experiments, the Anh-B sample was heated at 773 K for 2 h to confirm that this treatment heat did not change the crystal structure of the sample. The XRD data were collected at temperatures between 303 and 773 K with a 50 K interval in both the heating and cooling processes. At each fixed temperature, the diffraction pattern was taken for 50 min. The obtained diffraction patterns were analyzed by the Le Bail profile fitting method using RIETAN-FP software (Izumi and Momma 2007) to calculate lattice parameters.

Raman spectroscopy

The run product of Anh-B was fixed on a slide glass with epoxy resin and was well polished for Raman spectra measurements. A micro-Raman spectrometer (NRS–3100; JASCO) was used for the spectra measurements. The excitation light was a Nd:YAG laser with a wavelength of 532 nm. The slit width was 0.1 mm. The Raman shifts were

186 calibrated using trichloroethylene and a Ne lamp. The Raman spectrum was collected
187 by 3 rounds of 50-second exposures with an interval of 0.05 cm^{-1}. The measured
188 spectrum was analyzed using PeakFit software.
189
190 **Calorimetry**
191
192 Isobaric heat capacity (C_P) was measured using a differential scanning calorimeter
193 (DSC) (Diamond DSC; PerkinElmer) in the temperature range of 300–770 K. The
194 measurement temperature range was divided into four sections, i.e., 300–400, 380–480,
195 460–560 and 530–770 K. The ends of the temperature ranges of each section were
196 overlapped. The DSC temperature was calibrated with reference to the melting points of
197 indium, tin and zinc. The purge gas was nitrogen. In the temperature range of 300–560
198 K, data were obtained with a step of 5 K in the heating rate of 10 K min^{-1}. In the range
199 of 530−770 K, the step was 20 K with a heating rate of 20 K min^{-1}. The set of
200 measurements was repeated 4−7 times in each section, and the results at each
201 temperature were averaged. The data acquisition interval was one second. A special
202 reagent grade α-Al_2O_3 was used as the calorimetric standard. Prior to C_P measurements
203 of Anh-B, the C_P of Mg_2SiO_4 Fo was measured to confirm the accuracy of the

204 measurements, as done by Kojitani et al. (2012a). The sample weights were 9.970,
205 10.150 and 10.074 mg for Fo, α-Al_2O_3 and Anh-B, respectively. Each sample was
206 packed in an aluminum pan. A set of measurements for the empty pan, α-Al_2O_3, and Fo
207 or Anh-B was made over a single day run, and several measurements were made in the
208 above two temperature ranges. The measured heat data were analyzed by the enthalpy
209 method by Mraw and Naas (1979). The C_P of Fo and Anh-B were calibrated with
210 reference to those for α-Al_2O_3 obtained just before each measurement using the heat
211 capacity data for α-Al_2O_3 by Ditmars et al. (1982).

212 Low temperature C_P of Anh-B was measured by the thermal relaxation method
213 using a PPMS apparatus (Quantum Design). The C_P measurement was performed in the
214 temperature range of 2.0–302.6 K and at intervals of about 2 K. The sintered sample had
215 a weight of 10.988 mg and cylindrical shape with about 0.5 mm in height and 1 mm in
216 diameter. For better thermal contact, the surface at the bottom was flattened and
217 polished well. Apiezon N grease was placed between the sample and a sample platform
218 for the same purpose. More details of the measurement method are given in Akaogi et al.
219 (2007).

220

221

This is a preprint, the final version is subject to change, of the American Mineralogist (MSA)
Cite as Authors (Year) Title. American Mineralogist, in press.
(DOI will not work until issue is live.) DOI: http://dx.doi.org/10.2138/am-2017-6115

Results and discussion

High-pressure phase relations

Table 1 shows the results of high-pressure high-temperature experiments in $Mg_{14}Si_5O_{24}$, and the phase relations are illustrated in Figure 1. The phase boundary of Fo + Per = Anh-B was determined to be $P = 0.0013(8) \times T + 10.3(14)$ by least-squares fitting to the experimental data, where P and T are in GPa and K, respectively. This boundary is located at 1–3 GPa lower pressure than that of the Fo–Wd transition reported by Morishima et al. (1994). We found that Anh-B dissociates into a mixture of Wd + Per at 18–20 GPa and 1600–2100 K. The phase transition pressure at 2073 K was tightly constrained between 19.3 and 19.5 GPa by the normal and reverse runs. The least-squares fitting to the experimental data with a fixing point of 19.4 GPa and 2073 K provides the phase boundary equation of $P = 0.0025(5) \times (T–2073) + 19.4$. In addition, the high pressure-recovered sample from 22 GPa and 1873 K was a mixture of Rw + Per, not Wd + Per. This was consistent with the Wd–Rw transition boundary reported by Inoue et al. (2006), which was recalibrated using Tsuchiya's (2003) Au EoS. These results indicate that Anh-B is stable in a pressure range from 13 to 18 GPa around 1900

K. Our boundary of 5 Fo + 4 Per = Anh-B was placed at slightly higher pressure by 0.5–1.5 GPa than that determined by Ganguly and Frost (2006). This discrepancy is discussed later.

Using the powder X-ray diffraction data, lattice parameters and volume of Anh-B at room temperature and 1 atm were determined to be a = 5.8749(1) Å, b = 14.1969(2) Å, c = 10.0585(2) Å, V = 838.93(2) Å^3, i.e., molar volume of 252.61(1) cm^3/mol. All the determined lattice parameters and the volume showed good agreement with those of Crichton et al. (1999), while the lattice parameters were about 0.1% larger than those of Finger et al. (1991). Using our molar volume of Anh-B in combination with those of Mg_2SiO_4 Fo (43.66 cm^3/mol: Lager et al. 1981), Wd (40.53 cm^3/mol: Finger et al. 1993) and MgO Per (11.25 cm^3/mol: Tange et al. 2009), the volume changes at ambient conditions for the two reactions

$$5\ Mg_2SiO_4\ (Fo) + 4\ MgO\ (Per) = Mg_{14}Si_5O_{24}\ (Anh\text{-}B) \quad (1)$$

$$Mg_{14}Si_5O_{24}\ (Anh\text{-}B) = 5\ Mg_2SiO_4\ (Wd) + 4\ MgO\ (Per) \quad (2)$$

were determined to be –24.14 and –5.06 cm^3/mol; i.e., the density increases were 9.6% and 2.0%, respectively.

Thermal expansivity

258

259 The lattice parameters and cell volume of Anh-B determined by the
260 high-temperature XRD method are shown in Table 2. Figure 2 illustrates the measured
261 cell parameters and volumes as functions of temperature. At each temperature, the three
262 lattice parameters measured in both the heating and cooling processes agreed well,
263 within the range of experimental error. The volume data were used to obtain thermal
264 expansivity $\alpha = (1/V)(\partial V/\partial T)_P$. We examined three types of α expression: a constant, a
265 linear function $\alpha = a + bT$ and a polynomial $\alpha = a + bT + cT^{-2}$, where a, b and c are
266 parameters. The least-squares fittings of $\ln V = \ln V_0 + \int_{298}^{T} \alpha dT$, where V_0 and V are
267 volumes at 298 K and T K, respectively, gave the results of the constant α of
268 $3.07(4)\times10^{-5}$ K^{-1} and V_0 = 842.06(9) Å^3 (χ^2 = 0.040), the linear α of $2.24(27)\times10^{-5}$ +
269 $1.6(5)\times10^{-8}T$ K^{-1} and V_0 = 842.29(11) Å^3 (χ^2 = 0.026) and the α polynomial of
270 $2.4(16)\times10^{-5} + 1.4(21)\times10^{-8}T - 0.1(12)\times T^{-2}$ K^{-1} and V_0 = 842.30(13) Å^3 (χ^2 = 0.027). χ^2
271 represents a reduced chi-squared value calculated from the equation of
272 $\chi^2 = \left[\sum_i^n \frac{\left(V_i^{obs} - V_i^{calc}\right)^2}{\sigma_i^2}\right]/(n-m)$, where $V^{\mathrm{obs}}{}_i$ and σ_i are the measured volume and its
273 experimental error, respectively, $V^{\mathrm{calc}}{}_i$ is the calculated volume, and n and m are the
274 number of data points and the number of fitted parameters, respectively. Since α
275 expressed by the linear function of temperature had the smallest χ^2 and thus was the

most appropriate, we adopted it for the α experimentally determined in this study. Similarly, from the least-squares fittings to lattice parameter data, the linear expansivities (l) in the a-, b- and c-axis directions were determined as $l_a = 1.05(2) \times 10^{-5}$ K^{-1} ($\chi^2 = 0.024$), $l_b = 1.01(4) \times 10^{-5}$ K^{-1} ($\chi^2 = 0.217$) and $l_c = 1.01(4) \times 10^{-5}$ K^{-1} ($\chi^2 = 0.039$), respectively. Even if the linear function of temperature for the l expression is used, the obtained χ^2 values were almost the same as those by constant expression. The results indicate that thermal expansion of Anh-B crystal is isotropic. Figure 3 compares the obtained α with the α derived by Ottenello et al. (2010) using *ab initio* calculation. Within the temperature range of 300–770 K where the high-temperature XRD measurements were performed, our result was very consistent with that predicted by Ottonello et al. (2010)

Heat capacities and standard entropy

The results of high-temperature C_P measurements by DSC are summarized in Table 3, and graphed in Figure 4. The DSC measurements were performed in the temperature range of 300–770 K. For each 5 K interval in the temperature range of 300–560 K or each 20 K interval in the temperature range of 530–770 K, the mean temperature was

adopted as a measurement temperature. The C_P was measured 4–7 times at each temperature, and the average value was determined. The experimental uncertainties obtained from twice the standard deviation of the mean were less than 1.7%.

In Table 4 and Figure 4, the results of low-temperature C_P measurements using PPMS are shown. The experimental uncertainties are smaller than 2%. The data around 300 K are in very good agreement with those measured by DSC. This smooth correspondence between the DSC and PPMS data suggests the validity of both. The C_P polynomial adopted in Yong et al. (2006) and Akaogi et al. (2007),

$$C_P(T) = k_0 + k_1 T^{-0.5} + k_2 T^{-2} + k_3 T^{-3} + k_4 T + k_5 T^2 + k_6 T^3, \quad (3)$$

was fitted to the obtained C_P data where k_0–k_6 are coefficients. The fitting range was divided into four sections, 0–20, 20–70, 70–200 and 200–380 K. The curve fitting was individually performed in each section by the least-squares method. In the first section, $C_P = k_6 T^3$ was fitted to the C_P data because it is known that C_P is in proportion to the cubes of T in the temperature region close to zero. If data at a temperature higher than 22 K are included in the fitting, the goodness of fit goes down. Therefore, the upper limit of the first section was determined to be 20 K. In the second section, the C_P curve has a large curvature. For better fitting of such curves with large curvature, it is useful to withhold the inflection point seen around 115 K. For this reason, the upper limit of the

second section was set at 70 K. In the fourth section, since the errors in C_P data in the temperature range of 284.7–302.6 K were larger than the errors in the other PPMS data due to an anomalous heat effect from the grease used to improve the thermal contact, those C_P data were excluded from the fitting. To make the interpolation of this region with withheld data more reliable, the boundary between the third and fourth sections was set at 200 K and the C_P data up to 382.5 K measured by DSC were also included in the fitting. The polynomial for each section but the first was chosen by considering a reduced chi-squared value. Some of data were overlapped to provide a smooth correspondence with the neighboring polynomial at the section boundary. $C_P\,(T) = k_6T$ was fitted to the data in the range of 2.0–22.0 K, $C_P\,(T) = k_0 + k_2T^{-2} + k_4T + k_5T^{2}$ to the data in the range of 17.9–74.9 K, $C_P\,(T) = k_0 + k_1T^{-0.5} + k_2T^{-2} + k_3T^{-3} + k_4T + k_5T^{2}$ to the data in the range of 65.0–210.8 K and $C_P\,(T) = k_0 + k_1T^{-0.5} + k_2T^{-2} + k_3T^{-3}$ to the data in the range of 190.9–382.5 K. Coefficients derived from the fittings are given in Table 5 together with the reduced chi-squared (χ^2) and correlation factor (R^2) to indicate the goodness of fit. The degree of agreement between the measured data and the fitted curve in each section is also shown in Figure 4.

Once the low-temperature C_P is known, lattice vibrational entropy at 1 atm and 298.15 K ($S^{o}_{vib,298.15}$) can be calculated using the equation

$$S^{\circ}_{\mathrm{vib},298.15} = \int_0^{298.15} \frac{C_p}{T}\,\mathrm{d}T. \quad (4)$$

The fitted C_P polynomials shown in Table 5 were applied to this calculation. The $S^{o}_{\mathrm{vib},298.15}$ of Anh-B was determined to be 544.4(2) J/mol·K. The uncertainty of the entropy ($\delta_{S298.15}$) was obtained by propagation of the experimental errors in the measured C_P (δ_{Cpi}) from the following equation:

$$\delta^2_{S_{298.15}} = \sum_{i=1}^{n-1} \frac{1}{4}(T_{i+1} - T_i)^2 \left[\left(\frac{1}{T_i}\delta_{Cp_i}\right)^2 + \left(\frac{1}{T_{i+1}}\delta_{Cp_{i+1}}\right)^2\right] \quad (5)$$

where n is the number of the data points, and it was assumed that the uncertainties in measurement temperatures were negligibly small, namely $\delta_{Ti} = 0$. We adopted twice the $\delta_{S298.15}$ as the uncertainty of the obtained $S^{o}_{\mathrm{vib},298.15}$. According to the crystal structure analysis by Finger et al. (1991), we can assume no cation disorder in the Anh-B structure, i.e., no configurational entropy. Therefore, the standard entropy ($S^{o}_{298.15}$) is equal to $S^{o}_{\mathrm{vib},298.15}$. The experimentally determined $S^{o}_{298.15}$ is very close to the 547.3 J/mol·K estimated from the entropies of constituent oxides by Ganguly and Frost (2006), rather than the 561.2 J/mol·K derived by Ottonello et al. (2010) from *ab initio* calculations.

Raman spectrum

347

348 Figure 5a shows the measured Raman spectrum of Anh-B. The unit cell of Anh-B
349 contains two $Mg_{14}Si_5O_{24}$ units, namely, it contains 86 atoms. Therefore, the total degree
350 of freedom in lattice vibration was 258, with 3 of these 258 modes being acoustic
351 modes and the remaining 255 being optic modes. According to Ottonello et al. (2010),
352 the irreducible representation of the optic modes is given as

353 $$\Gamma_{opt} = 35A_g + 25B_{1g} + 35B_{2g} + 25B_{3g} + 28A_u + 40B_{1u} + 27B_{2u} + 40B_{3u} \quad (6)$$

354 with an axis setting of the space group *Pmcb*. The optic modes consist of 120 gerade
355 modes which are Raman active and 135 ungerade modes which are infrared (IR) active
356 or silent. In this study, 36 Raman peaks were observed, and their wave numbers are
357 listed in Table 6. Figure 5a also includes wave numbers of the 255 optic modes obtained
358 by the *ab initio* calculation of Ottenello et al. (2010). The vibrational mode frequencies
359 of the observed Raman peaks were generally consistent with those of the calculated
360 optic modes. This suggests that the distribution of the wave numbers at Γ-point for all
361 the calculated optic modes is acceptable. In the next section, we use the distribution of
362 the vibrational mode frequencies to model a vibrational density of state (VDoS) for the
363 lattice vibrational model calculation.

364

365 **Calculation of heat capacity**

366

367 The high-temperature heat capacity of Anh-B above 760 K was extrapolated using
368 lattice vibrational model calculation with the Kieffer model (Kieffer 1979a, 1979b), in
369 which the heat capacity at constant volume (C_V) is calculated by modeling the phonon
370 density of state for acoustic and optic modes.

371 To calculate the contribution of the acoustic modes to C_V, directionally averaged
372 sound velocities (u_1, u_2, u_3) are used, which are derived from compressional and shear
373 wave velocities, v_p and v_s, respectively. The u_1 and u_2 are slower and faster transverse
374 wave velocities, respectively, and the u_3 is a longitudinal wave velocity. In the manner
375 of Kojitani et al. (2003), we estimated the compressional velocity (v_p) of Anh-B using
376 Birch's (1961) law between v_p in km/s and density (ρ) in g/cm^3, $v_p = -1.87 - 0.7(m-21) + 3.05\rho$, where m is a mean atomic weight. v_s was calculated from
378 $v_s = \sqrt{\frac{3}{4}\left(v_p{}^2 - K_S/\rho\right)}$, where K_S is the adiabatic bulk modulus, and it was assumed that
379 K_S was equivalent to the isothermal bulk modulus (K_T). The directionally averaged
380 sound velocities were calculated from the v_p and v_s using the method of Kieffer (1979a).
381 The u_1, u_2 and u_3 were determined to be 4.866, 6.671 and 9.194 km/s, respectively.

382 We adopted a four optic-continua model with wave-number ranges of 187–540,

383 540–700, 790–910 and 950–1050 cm^{-1}, which contained 190, 33, 26 and 6 optic modes,
384 respectively, based on the measured Raman spectrum and the vibrational mode
385 calculations by Ottonello et al. (2010). The vibrational density of state model is
386 illustrated in Figure 5b, and the parameters used for the Kieffer model calculation are
387 summarized in Table 7. Because, in general, C_V will be approximately equal to C_P at all
388 temperature below 200 K, the lower cutoff frequency of the first optic continuum,
389 which largely affects the calculated low-temperature C_V value, was adjusted to
390 reproduce the measured low-temperature C_P up to 200 K. The obtained C_V are listed in
391 Table 8.
392
393 **High-temperature extrapolation of thermal expansivity**
394
395 Since the α determined by the high-temperature XRD measurement was limited up
396 to 773 K in this study, the experimentally determined values of α were extrapolated to
397 higher temperature using the Grüneisen relation equation
398 $$\alpha(T) = \frac{\gamma_{th} C_V(T)}{K_T(T) V_0(T)} , \quad (7)$$
399 where γ_{th}, $C_V(T)$, $K_T(T)$ and $V_0(T)$ represent the thermal Grüneisen parameter, isochoric
400 heat capacity, isothermal bulk modulus and volume at T K and ambient pressure,

401 respectively. The C_V values obtained in the previous section were applied to this
402 calculation. K_T at T K was obtained by the equation

403 $$K_T(T) = K_T(298) + \left(\frac{\partial K_T}{\partial T}\right)_P (T - 298), \quad (8)$$

404 where $(\partial K_T/\partial T)_P$ is a temperature derivative of K_T at constant pressure. Since there was
405 no experimentally determined $(\partial K_T/\partial T)_P$ for Anh-B, the value was estimated from the
406 equation proposed by Anderson (1995):

407 $$\left(\frac{\partial K_T}{\partial T}\right)_P = -\overline{\alpha K_T} \cdot (K_T{}' - q^{ht} + 1), \quad (9)$$

408 where $\overline{\alpha K_T}$ and $K_T{}'$ refer to an averaged αK_T and pressure derivative of K_T,
409 respectively. q^{ht} is a parameter defined by the following equation:

410 $$q^{ht} = \frac{\partial\, ln\gamma^{ht}}{\partial\, lnV} \quad (10)$$

411 where γ^{ht} is a Grüneisen parameter at high temperature. In the present study, the q^{ht}
412 value was approximated to be unity (Anderson 1995). $V_0(T)$ was calculated by the
413 equation:

414 $$V_0(T) = V_0(298) \cdot exp\left[\int_{298}^{T} \alpha\, dT\right]. \quad (11)$$

415 As shown in Equations 9 and 11, the calculations of $(\partial K_T/\partial T)_P$ and $V_0(T)$ include α.
416 Therefore, α was calculated using the iteration calculation method with an initial $V_0(T)$,
417 keeping $V_0(298)$ constant, and an initial $(\partial K_T/\partial T)_P$ of a proper value. The final $(\partial K_T/\partial T)_P$
418 thus obtained does not depend on the initial value. Five iterations provided a converged

419 α. The detailed methods used for the iteration calculation of α are described in Kojitani
420 et al. (2012b).

421 Since the γ_{th} of Anh-B has not yet been tightly constrained, we calculated a different
422 α using different γ_{th} values of 1.1, 1.2 and 1.3 at 298 K by adopting $K_T(298)$ of 151.5
423 GPa and K_T' of 5.5 as reported by Crichton et al. (1999) and a $V_0(298)$ of 252.61
424 cm^3/mol as obtained in the present study, where the volume dependency, i.e., practical
425 temperature dependency, of γ_{th} was included with consideration for the q^{ht} value of unity
426 as shown in Equation 10. The results of the calculations are shown in Figure 3. In the
427 temperature range of 300–800 K, the α calculated with a γ_{th} of 1.2 is in very good
428 agreement with that determined by the present high-temperature XRD measurement.
429 Therefore, we adopted the α obtained with a γ_{th} of 1.2, which gave an $(\partial K_T/\partial T)_P$ of –
430 0.0275 GPa/K. The α calculated with a γ_{th} of 1.2 was also consistent with that of
431 Ottonello et al. (2010) below 800 K. However, above 800 K the former was larger than
432 the latter and the difference between them became larger with increasing temperature.

433

434 **Isobaric heat capacity calculation**

435

436 The isobaric heat capacity (C_P) is calculated within the quasi-harmonic

437 approximation from the equation

438 $$C_P(T) = C_V(T) + \alpha(T)^2 K_T(T) V_0(T) T \,. \quad (12)$$

439 The physical properties used for the C_P calculation of Anh-B are summarized in Table 9.
440 The calculated C_P values of Anh-B are listed in Table 8 together with C_V and α, and they
441 are also shown in Figure 6 in comparison with the measured C_P values in this study and
442 those predicted by Ottonello et al. (2010). The calculated C_P values well-reproduced not
443 only the C_P data up to about 300 K by PPMS but also those by DSC within the
444 experimental uncertainties. The present C_P calculation result was quite close to that of
445 Ottonello et al. (2010) over the temperature range of the calculation; nonetheless, the
446 former was up to 0.7% higher than the latter. This was mostly due to the higher α of the
447 present study compared to that of Ottonello et al. (2010), as shown in Figure 3.

448

449

450 **Calculation of the phase boundaries on Anh-B**

451

452 Thermodynamic calculations of the phase equilibrium boundaries for the reactions
453 of Equations 1 and 2 were performed by applying the thermodynamic properties of
454 Anh-B obtained in this study, using the following equation:

$$\Delta G(P,T) = \Delta H^{\circ}{}_{\mathrm{t}}(T) - T \cdot \Delta S^{\circ}(T) + \int_{1\,\mathrm{atm}}^{P} \Delta V(p,T)\,\mathrm{d}\,p = 0, \quad (13)$$

where $\Delta H^{\circ}{}_{\mathrm{t}}(T)$ and $\Delta S^{\circ}(T)$ are the enthalpy and entropy of a phase transition at 1 atm and T K, respectively, and $\Delta V(p,T)$ is the volume change at p GPa and T K. The $\Delta H^{\circ}{}_{\mathrm{t}}(T)$ and $\Delta S^{\circ}(T)$ were calculated using $\Delta H^{\circ}{}_{\mathrm{t}}(298)$, $\Delta S^{\circ}(298)$ and isobaric heat capacities at 1 atm, C_P, as shown by the following equations:

$$\Delta H^{\circ}{}_{\mathrm{t}}(T) = \Delta H^{\circ}{}_{\mathrm{t}}(298) + \int_{298}^{T} \Delta C_P(T')\,\mathrm{d}\,T' \quad (14)$$

$$\Delta S^{\circ}(T) = \Delta S^{\circ}(298) + \int_{298}^{T} \frac{\Delta C_P(T')}{T'}\,\mathrm{d}\,T'. \quad (15)$$

Volumes at given pressures and temperatures, V, were calculated using a third-order high-temperature Birch–Murnaghan equation of state (EoS) or a Mie–Grüneisen–Debye EoS. The third-order high-temperature Birch–Murnaghan EoS is represented as

$$P_T(V) = \frac{3}{2} K_T(T) \cdot \left[\left(\frac{V}{V_0(T)} \right)^{-7/3} - \left(\frac{V}{V_0(T)} \right)^{-5/3} \right] \cdot \left\{ 1 + \frac{3}{4} \left(K'_T - 4 \right) \cdot \left[\left(\frac{V}{V_0(T)} \right)^{-2/3} - 1 \right] \right\} \quad (16)$$

where $P_T(V)$ represents the pressure as a function of V at T K and $V_0(T)$ is the volume at 1 atm and T K. On the other hand, the Mie–Grüneisen–Debye EoS is expressed as

$$P_T(V) = P_{298}(V) + \frac{\gamma(V)}{V} \left[E_{\mathrm{th}}(V,T) - E_{\mathrm{th}}(V,298) \right] \quad (17)$$

where γ and E_{th} are a Grüneisen parameter and the internal thermal energy, respectively. The $P_{298}(V)$ term was calculated using Equation 16 or a Vinet EoS:

$$P_T(V) = 3K_T(T) \cdot \left(\frac{V}{V_0(T)}\right)^{-2/3} \left[1 - \left(\frac{V}{V_0(T)}\right)^{1/3}\right] \cdot \exp\left\{\frac{3}{2}\left(K'_T - 1\right) \cdot \left[1 - \left(\frac{V}{V_0(T)}\right)^{1/3}\right]\right\} \quad . \tag{18}$$

$E_{th}(V,T)$ was obtained from the Debye model as follows:

$$E_{th}(V,T) = 9nRT\left[\frac{\theta_D(V)}{T}\right]^{-3} \int_0^{\theta_D(V)/T} \frac{x^3}{e^x - 1} dx \tag{19}$$

where n, R and θ_D are the number of atoms per formula, the gas constant and a Debye temperature, respectively. The models for γ and θ_D are expressed as

$$\gamma(V) = \gamma_0 \left\{1 + k\left[\left(\frac{V}{V_0}\right)^q - 1\right]\right\} \tag{20}$$

$$\theta_D(V) = \theta_{D0}\left(\frac{V}{V_0}\right)^{-\gamma_0(1-k)} \times \exp\left[-\frac{\gamma(V) - \gamma_0}{q}\right] \tag{21}$$

by following the equations of Tange et al. (2009), where γ_0 and θ_{D0} represent γ and θ_D at V_0, respectively, and q and k are constants.

Prior to the phase boundary calculations of the reactions of Equations 1 and 2, we performed thermodynamic calculations of the Fo–Wd and Wd–Rw phase transition boundaries to optimize enthalpy data and check the reliability of the other thermodynamic parameters for Fo and Wd. Thermodynamic parameters for the three phases are listed in Table 9.

Since α, C_P and $(\partial K_T/\partial T)_P$ of Wd have not yet been well constrained, we optimized

488 them using the same approach as for Anh-B. C_V of Wd was calculated by the Kieffer
489 model calculation using the VDoS model shown in Table 7, which reproduces the
490 low-temperature C_P data measured by Akaogi et al. (2007). The calculated C_V of Wd are
491 given in Table 8 and Figure 7. The obtained C_V was applied to α, $(\partial K_T/\partial T)_P$ and C_P
492 calculations. In the α calculation, a γ_{th} of 1.3 was used because it gave consistent α with
493 the α values measured by Suzuki et al. (1980) and Trots et al. (2012) below 1000 K, as
494 shown in Figure 8. At the same time, the γ_{th} of 1.3 provided $(\partial K_T/\partial T)_P$ of –0.0237
495 GPa/K. The C_P calculated using the obtained C_V, α and $(\partial K_T/\partial T)_P$ are given in Table 8
496 and Figure 7. The present calculations yielded 3–4% higher C_P values than the previous
497 DSC measurements by Watanabe (1982) and Ashida et al. (1987), which were rather
498 comparable to the C_V values calculated in this study.

499 Phase transition enthalpies at 298 K [$\Delta H^o_t(298)$] for the Fo–Wd and Wd–Rw
500 transitions can be obtained using drop-solution enthalpies ($\Delta H_{d\text{-}s}$) of the three phases. In
501 the drop-solution enthalpy measurement, a material is dropped from outside of a
502 calorimeter at room temperature into molten oxide solvent inside the calorimeter at high
503 temperature, and the enthalpy difference between the crystalline state at room
504 temperature and dissolution state in the solvent at high temperature is measured. In this
505 approach, materials with the same composition can be assumed to have the same

506 dissolution state; for example, $\Delta H^{o}_{t}(298)$ of the Fo–Wd transition is calculated from
507 $\Delta H_{d\text{-}s}(\mathrm{Fo}) - \Delta \mathrm{H}_{d\text{-}s}(\mathrm{Wd})$ (cf., Akaogi et al. 2007). In Table 10, drop-solution enthalpies of
508 the related materials in $2\mathrm{PbO}\cdot\mathrm{B_2O_3}$ solvent at 978 K are summarized. The internal
509 consistency of $\Delta H_{d\text{-}s}$ data among Fo, Per and $\mathrm{SiO_2}$ quartz has already been confirmed in
510 Kojitani et al. (2016). Therefore, the $\Delta H_{d\text{-}s}$ data for Fo and Per by Kojitani et al. (2016)
511 were used. Since $\Delta H_{d\text{-}s}(\mathrm{Rw})$ has also been well constrained from the data by Akaogi et
512 al. (2007) and Kojitani et al. (2016), we adopted the average of their $\Delta H_{d\text{-}s}(\mathrm{Rw})$ values.
513 For $\Delta H_{d\text{-}s}(\mathrm{Wd})$, only the value measured by Akaogi et al. (2007) was used. The phase
514 equilibrium boundaries calculated by adopting $\Delta H_{d\text{-}s}$ of 168.2 ± 0.4 kJ/mol for Fo, 142.2
515 ± 1.3 kJ/mol for Wd and 129.0 ± 1.0 kJ/mol for Rw, which give $\Delta H^{o}_{t}(298)$ of 26.0 ± 1.4
516 kJ/mol for the Fo–Wd transition and 13.2 ± 1.6 kJ/mol for the Wd–Rw transition, are
517 shown in Figure 9. The calculated Fo–Wd boundary agrees well with that by the
518 high-pressure and high-temperature in situ experiments of Morishima et al. (1994).
519 On the other hand, the calculated Wd–Rw boundary is also consistent with those
520 determined by the high-pressure and high-temperature in situ experiments of Inoue et al.
521 (2006) and Suzuki et al. (2000), where the pressure data of Inoue et al. (2006) were
522 re-scaled using Tsuchiya's (2003) Au EoS. These findings confirm the validity of the
523 thermodynamic parameters used for Fo and Wd.

524 $\Delta H^{o}_{t}(298)$ for the reactions of Equations 1 and 2 are obtained from 5 $\Delta H_{d\text{-}s}$(Fo) + 4
525 $\Delta H_{d\text{-}s}$(Per) – $\Delta H_{d\text{-}s}$(Anh-B) and $\Delta H_{d\text{-}s}$(Anh-B) – 5 $\Delta H_{d\text{-}s}$(Wd) – 4 $\Delta H_{d\text{-}s}$(Per), respectively.
526 Measured $\Delta H_{d\text{-}s}$ data of Anh-B have not been yet reported, because it is difficult to
527 synthesize the large amount of single-phase sample required for drop-solution
528 calorimetry. For this reason, the phase boundary calculations of the reactions of
529 Equations 1 and 2 were performed using the expected $\Delta H_{d\text{-}s}$ values of Anh-B in the
530 range from 904 to 912 kJ/mol at intervals of 2 kJ/mol. The results of the calculations are
531 shown in Figure 10. A higher $\Delta H_{d\text{-}s}$(Anh-B) value results in a lower transition pressure
532 for the reaction of Equation 1 and a higher one for the reaction of Equation 2, as shown
533 in Figures 10a and 10b, respectively. The transition pressure of the latter is especially
534 sensitive to the $\Delta H_{d\text{-}s}$(Anh-B) values. It is important to note that both of the
535 experimentally determined boundaries can be explained within the experimental errors
536 by the thermodynamic calculations using the same $\Delta H_{d\text{-}s}$(Anh-B) of 908 ± 1 kJ/mol.
537 As described earlier, the experimentally determined transition pressure for the
538 reaction of Equation 1 is about 1 GPa higher than that of Ganguly and Frost (2006). The
539 calculation with $\Delta H_{d\text{-}s}$(Anh-B) of 917 kJ/mol gives a phase boundary very close to that
540 reported by Ganguly and Frost (2006), as shown in Figure 10a. However, when the
541 same $\Delta H_{d\text{-}s}$(Anh-B) is applied to the phase boundary calculation of the reaction of

Equation 2, the transition pressure is calculated to be 22.2 GPa at 1873 K, which is much higher than the value of about 18.5 GPa determined experimentally in this study, and is beyond the phase stability region of Wd (Figure 10b). On the other hand, although the boundary for the reaction in Equation 1 calculated by Ottonello et al. (2010) is consistent with both our high-pressure experimental data above 1873 K and the thermodynamic calculation with $\Delta H_{\text{d-s}}$(Anh-B) of about 913 kJ/mol, the boundary by Ottonello et al. (2010) does not agree with the high-pressure experimental data at 1673 K. This discrepancy is probably attributable to the fact that the $S^{\circ}_{298.15}$ of Anh-B (561.2 J/mol·K) estimated by Ottonello et al. (2010) is higher than that measured in this study (544.4 J/mol·K) because the higher $S^{\circ}_{298.15}$ of Anh-B results in a steeper Clapeyron slope. Therefore, the present phase boundary would appear to be more appropriate than the previous ones for the reaction of Equation 1.

From the above discussion on the phase boundaries, it is concluded that, in the $Mg_{14}Si_5O_{24}$ system, Anh-B is stable in the pressure range from 13 to 18 GPa at 1873 K. In addition, $\Delta H_{\text{d-s}}$(Anh-B) is expected to be around 908 kJ/mol, suggesting that the formation enthalpy from elements at the standard state ($\Delta_f H^{\circ}_{298}$) is –13208 kJ/mol, as calculated from the enthalpy difference between 5 Fo + 4 Per and Anh-B and $\Delta_f H^{\circ}_{298}$ values of Fo and Per listed in Table 9.

This is a preprint, the final version is subject to change, of the American Mineralogist (MSA)
Cite as Authors (Year) Title. American Mineralogist, in press.
(DOI will not work until issue is live.) DOI: http://dx.doi.org/10.2138/am-2017-6115

560

561

562 **Implications**

563

564 The stability field of Anh-B in the $Mg_{14}Si_5O_{24}$ system was thermodynamically
565 calculated in the temperature range of 300–2700 K and the pressure range of 10–21 GPa
566 using the optimized $\Delta H_{d\text{-}s}$(Anh-B) of 908 kJ/mol, namely $\Delta_f H^o_{298}$(Anh-B) of –13208
567 kJ/mol. The thermodynamic parameters used are listed in Table 9. Our thermodynamic
568 calculation results shown in Figure 11 indicate that the stability field of Anh-B places
569 between 5 Fo + 4 Per and 5 Wd + 4 Per with a 3–7 GPa interval over the whole
570 calculation temperature range of 300–2700 K. The interval of pressure of the Anh-B
571 stability field becomes narrower with increasing temperature. This suggests that Anh-B
572 can be stable in relatively wide pressure and temperature ranges if the local bulk
573 composition of a mantle rock is enriched with an MgO component because of, for
574 example, selective dissolution of the Si component into fluid. Furthermore, in the
575 Mg_2SiO_4–$MgCr_2O_4$ system, it is expected that the Cr-bearing Anh-B synthesized by
576 Bindi et al. (2016) would also be allowed to exist in a similar pressure range between 13
577 and 18 GPa at 1873 K if it is assumed that the effect of the Cr component on the

578 stability pressure is negligibly small.

579 Presnall and Gasparik (1990) observed the coexistence of Anh-B with silica-rich
580 liquid in the Mg_2SiO_4 system under the conditions of 16.5 GPa and 2623 K. This
581 temperature was about 100 K higher than the upper temperature limit of the stability
582 field of Anh-B at 16.5 GPa (Figure 11). However, the higher temperature limit at 16.5
583 GPa becomes 80 K higher with the use of $\Delta_f H^o_{298}$ (Anh-B) of –13211 kJ/mol, which is
584 just 3 kJ/mol larger than the –13208 kJ/mol optimized in this study. Therefore, it is
585 likely that the result of Presnall and Gasparik (1990) is consistent with our calculated
586 stability field of Anh-B, when considering both the errors in their high-pressure and
587 high-temperature experiment and our thermodynamic calculations.

588 Seismic discontinuities in the 250–350 km depth range in the Earth's upper mantle,
589 or so-called X-discontinuity, have been observed beneath regions of the subduction zone
590 and continents (e.g., Schmarr et al. 2013). The depth range corresponds to a pressure
591 range of 8–11.5 GPa. If we consider that fluid in subducting slabs is enriched in the
592 SiO_2 component, it is possible that the reaction of 5 Fo + 4 Per = Anh-B proceeds in the
593 residual rock enriched with the MgO component. When we consider the slabs with an
594 internal temperature range of 800–1500 K at around 300-km depth as estimated by, e.g.,
595 Kirby et al. (1996), the reaction occurs at a pressure of 10–12 GPa based on our results

shown in Figure 11. As Ganguly and Frost (2006) suggested, the effect of water on the phase boundary can reduce the pressure of the reaction by about 1 GPa. By taking this effect into account, it is likely that the reaction occurs at 9–11 GPa under wet conditions. The obtained pressure range of the reaction overlaps with that of the X-discontinuity. Therefore, the reaction 5 Fo + 4 Per = Anh-B under wet conditions would be another candidate for the X-discontinuity, in addition to the coesite–stishovite phase transition in SiO_2 (Williams and Revenaugh 2005), the hydrous phase A formation (Akaogi and Akimoto 1980) and the orthorhombic to high-pressure monoclinic phase transition in pyroxene (Woodland 1998).

We also performed thermodynamic calculations of the high-pressure high-temperature phase relation in the $Mg_{14}Si_7O_{28}$ (i.e., Mg_2SiO_4) system to examine the stability field of Anh-B + 2 St. In these calculations, Gibbs free energies at given *P*–*T* conditions for Fo, Wd, Rw, 14 Per + 7 St, and Anh-B + 2 St were compared in the pressure range of 10–21 GPa and the temperature range of 800–2500 K. The results of the calculations are shown in Figure 12. We found that the Anh-B + 2 St field was stable when $\Delta_f H^o_{298}$(Anh-B) values negatively larger than –13235 kJ/mol were adopted. The Anh-B + 2 St field has a lens-like shape along the phase boundary between Wd and Rw. It starts to appear at around 17 GPa and 800 K. The stability pressure is higher than that

of about 15 GPa previously suggested by Ganguly and Frost (2006). As described above, the $\Delta_f H^o_{298}$(Anh-B) value of –13235 kJ/mol is too large to explain the phase boundaries for 5 Fo + 4 Per = Anh-B and Anh-B = 5 Wd + 4 Per determined by our high-pressure experiments. When a $\Delta_f H^o_{298}$(Anh-B) of around –13208 kJ/mol is adopted, the stability field of Anh-B + 2 St never appears under any *P*–*T* conditions. The calculation results thus suggest that Anh-B would not be formed in peridotites under subsolidus and anhydrous conditions. If the local bulk compositions of such rocks are enriched with an MgO component or the Gibbs free energy of Anh-B is effectively reduced by some other components, Anh-B might possibly exist in mantle peridotites.

Acknowledgments

We thank P.D. Asimow for helpful review comments. This work was supported in part by the JSPS grants (No. 15K05347 to H. K. and No. 25287145 and No. 17H02986 to M. A.) and by the MEXT-supported program for the Strategic Research Foundation at Private Universities.

References

Akaogi, M., and Akimoto, S. (1980) High-pressure stability of a dense hydrous magnesian silicate $Mg_{23}Si_8O_{42}H_6$ and some geophysical implications. Journal of Geophysical Research, 85, 6944–6948.

Akaogi, M., Yusa, H., Shiraishi, K., and Suzuki, T. (1995) Thermodynamic properties of α-quartz, coesite, and stishovite and equilibrium phase relations at high pressures and high temperatures. Journal of Geophysical Research, 100, 22337–22347.

Akaogi, M., Takayama, H., Kojitani, H., Kawaji, H., and Atake, T. (2007) Low-temperature heat capacities, entropies and enthalpies of Mg_2SiO_4 polymorphs, and α–β–γ and post-spinel phase relations at high pressure. Physics and Chemistry of Minerals, 34, 169−183.

Akaogi, M., Oohata, M., Kojitani, H., and Kawaji, H. (2011) Thermodynamic properties of stishovite by low-temperature heat capacity measurements and the coesite–stishovite transition boundary. American Mineralogist, 96, 1325–1330.

Anderson, O.L. (1995) Equations of state of solids for geophysics and ceramic science. Oxford monographs on geology and geophysics, No. 31, Oxford University Press, New York.

650 Arai, S. (1997) Control of wall–rock composition on the formation of podiform
651 chromitites as a result of magma/peridotite interaction. Resource Geology, 47, 177–
652 187.
653 Arai, S. and Miura, M. (2016) Formation and modification of chromitites in the mantle.
654 Lithos, 264, 277–295.
655 Ashida, T., Kume, S., and Ito, E. (1987) Thermodynamic aspects of phase boundary
656 among α-, β- and γ-Mg_2SiO_4, In: M.H. Manghnani and Y. Syono, Eds., High-pressure
657 research in mineral physics, p. 269−274. Terra Scientific Publishing, Tokyo/
658 American Geophysical Union, Washington D.C.
659 Bindi, L., Sirotkina, E.A., Bobrov, A.V., Nestola, F., and Irifune, T. (2016) Chromium
660 solubility in anhydrous Phase B. Physics and Chemistry of Minerals, 43, 103–110.
661 Birch, F. (1961) The velocity of compressional waves in rocks to 10 kilobars, part 2.
662 Journal of Geophysical Research, 66, 2199–2224.
663 Crichton, W.A., Ross, N.L., and Gasparik, T. (1999) Equations of state of magnesium
664 silicates anhydrous B and superhydrous B. Physics and Chemistry of Minerrals, 26,
665 570–575.
666 Ditmars, D.A., Ishihara, S., Chang, S.S., Bernstein, G., and West, E.D. (1982) Enthalpy
667 and heat-capacity standard reference material: synthetic sapphire (α-Al_2O_3) from 10

668 to 2250 K. Journal of Research of the National Bureau of Standards, 87, 159−163.

669 Dunn, K.J. and Bundy, F.P. (1978) Materials and techniques for pressure calibration by

670 resistance-jump transitions up to 500 kilobars. Review of Scientific Instruments, 49,

671 365−370.

672 Fei, Y., Mao, H.K., Shu, J., Parthasarathy, G., Bassett W.A., and Ko, J. (1992)

673 Simultaneous high-P, high-T X ray diffraction study of β-$(Mg,Fe)_2SiO_4$ to 26 GPa

674 and 900 K. Journal of Geophysical Research, 97, 4489–4495.

675 Finger, L.W., Ko, J., Hazen, R.M., Gasparik, T., Hemley, R.J., Prewitt, C.T., and

676 Weidner, D.J. (1989) Crystal chemistry of phase B and an anhydrous analogue:

677 implications for water storage in the upper mantle. Nature, 341, 140–142.

678 Finger, L.W., Hazen, R.M., and Prewitt, C.T. (1991) Crystal structures of

679 $Mg_{12}Si_4O_{19}(OH)_2$ (phase B) and $Mg_{14}Si_5O_{24}$ (phase AnhB). American Mineralogist,

680 76, 1–7.

681 Finger, L.W., Hazen, R.M., Zhang, J., Ko, J., and Navrotsky, A. (1993) The effect of Fe

682 on the crystal structure of wadsleyite β-$(Mg_{1-x}Fe_x)_2SiO_4$, $0.00 \leq x \leq 0.40$. Physics and

683 Chemistry of Minerals, 19, 361–368.

684 Ganguly, J. and Frost, D.J. (2006) Stability of anhydrous phase B: Experimental studies

685 and implications for phase relations in subducting slab and the X discontinuity in the

686 mantle. Journal of Geophysical Research, 111, B06203.

687 Herzberg, C.H. and Gasparik, T. (1989) Melting experiments on chondrite at high
688 pressures: Stability of anhydrous B. Eos Trans., AGU, 70, 484.

689 Inoue, T., Irifune, T., Higo, Y., Sanehira, T., Sueda, Y., Yamada, A., Shinmei, T.,
690 Yamazaki, D., Ando, J., Funakoshi, K., and Utsumi, W. (2006) The phase boundary
691 between wadsleyite and ringwoodite in Mg_2SiO_4 determined by in situ X-ray
692 diffraction. Physics and Chemistry of Minerals, 33, 106–114.

693 Ito, E., 2007. Theory and practice – Multianvil cells and high-pressure experimental
694 methods. In: G.D. Price, Ed., Mineral Physics, 2, p. 197–230. Treatise on Geophysics,
695 Elsevier, Amsterdam.

696 Izumi, F. and Momma, K. (2007) Three-dimensional visualization in powder diffraction.
697 Solid State Phenomena, 130, 15–20.

698 Jacobs, M.H.G. and Oonk, H.A.J. (2001) The Gibbs energy formulation of the α, β, and
699 γ forms of Mg_2SiO_4 using Grover, Getting and Kennedy's empirical relation between
700 volume and bulk modulus. Physics and Chemistry of Minerals, 28, 572–585.

701 Kajiyoshi, K (1986) High-temperature equation of state for mantle minerals and their
702 anharmonic properties. MS Thesis, Okayama University, Okayama, Japan.

703 Kieffer, S.W. (1979a) Thermodynamics and lattice vibrations of minerals: 1. Mineral

heat capacities and their relationships to simple lattice vibrational models. Reviews of Geophysics and Space Physics, 17, 1−19.

Kieffer, S.W. (1979b) Thermodynamics and lattice vibrations of minerals: 3. Lattice dynamics and an approximation for minerals with application to simple substances and framework silicates. Reviews of Geophysics and Space Physics, 17, 35−59.

Kirby, S.H., Stein, S., Okal, E.A., and Rubie, D.C. (1996) Metastable mantle phase transformations and deep earthquakes in subducting oceanic lithosphere. Reviews of Geophysics, 34, 261−306.

Kojitani, H., Nishimura, K., Kubo, A., Sakashita, M., Aoki, K., and Akaogi, M. (2003) Raman spectroscopy and heat capacity measurement of calcium ferrite type $MgAl_2O_4$ and $CaAl_2O_4$. Physics and Chemistry of Minerals, 30, 409–415.

Kojitani, H., Oohata, M., Inoue, T., and Akaogi, M. (2012a) Redetermination of high-temperature heat capacity of Mg_2SiO_4 ringwoodite: Measurement and lattice vibrational model calculation. American Mineralogist, 97, 1314–1319.

Kojitani, H., Ishii, T., and Akaogi, M. (2012b) Thermodynamic investigation on phase equilibrium boundary between calcium ferrite-type $MgAl_2O_4$ and MgO + α-Al_2O_3. Physics of the Earth and Planetary Interiors, 212–213, 100–105.

Kojitani, H., Inoue, T., and Akaogi, M. (2016) Precise measurements of enthalpy of

722 postspinel transition in Mg_2SiO_4 and application to the phase boundary calculation.
723 Journal of Geophysical Research Solid Earth, 121, 729–742.
724 Lager, G.A., Ross, F.K., and Rotella, F.J. (1981) Neutron powder diffraction of forsterite,
725 Mg_2SiO_4: a comparison with single-crystal investigations. Journal of Applied
726 Crystallography, 14, 137–139.
727 Morishima, H., Kato, T., Suto, M., Ohtani, E., Urakawa, U., Shimomura, O., and
728 Kikegawa, T. (1994) The phase boundary between α- and β-Mg_2SiO_4 determined by
729 in situ X-ray observation. Science, 265, 1202–1203.
730 Mraw, S.C. and Naas, D.F. (1979) The measurement of accurate heat capacities by
731 differential scanning calorimetry. Comparison of d.s.c. results on pyrite (100 to 800
732 K) with literature values from precision adiabatic calorimetry. Journal of Chemical
733 Thermodynamics, 11, 567−584.
734 Nishihara, Y., Nakayama, K., Takahashi, E., Iguchi, T., and Funakoshi, K. (2005) *P–V–T*
735 equation of state of stishovite to the mantle transition zone conditions. Physics and
736 Chemistry of Minerals, 31,660–670.
737 Ono, S., Katsura, T., Ito, E., Kanzaki, M., Yoneda, A., and Walter, M.J. (2001) In situ
738 observation of ilmenite-perovskite phase transition in $MgSiO_3$ using synchrotron
739 radiation. Geophysical Research Letters, 28, 835–838.

740 Ottonello, G., Civalleri, B., Ganguly, J., Perger, W.F., Belmonte, D., and Vetuschi
741 Zuccolini, M. (2010) Thermo-chemical and thermo-physical properties of the
742 high-pressure phase anhydrous B ($Mg_{14}Si_5O_{24}$): An ab-initio all-electron investigation.
743 American Mineralogist, 95, 563–573.
744 Presnall, D.C. and Gasparik, T. (1990) Melting of enstatite ($MgSiO_3$) from 10 to 16.5
745 GPa and the forsterite (Mg_2SiO_4)–majorite ($MgSiO_3$) eutectic at 16.5 GPa:
746 Implications for the origin of the mantle. Journal of Geophysical Research, 95,
747 15771–15777.
748 Robie, R.A. and Hemingway, B.S. (1995) Thermodynamic properties of minerals and
749 related substances at 298.15 K and 1 bar (10^5 Pascals) pressure and at higher
750 temperatures, 461 p. US Geological Survey Bull 2131.
751 Sasaki, S., Prewitt, C.T., Sato, Y., and Ito, E. (1982) Single-crystal X-ray study of
752 γ-Mg_2SiO_4. Journal of Geophysical Research, 87, 7829−7832.
753 Schmarr, N.C., Kelly, B.M., and Thorne, M.S. (2013) Broadband array observations of
754 the 300 km seismic discontinuity. Geophysical Research Letters, 40, 841–846.
755 Suzuki, I., Ohtani, E., and Kumazawa, M. (1980) Thermal expansion of modified
756 spinel , β-Mg_2SiO_4. Journal of Physics of the Earth, 28, 273–280.
757 Suzuki, A., Ohtani, E., Morishima, H., Kubo, T., Kanbe, Y. Kondo, T., Okada, T.,

758 Terasaki, H., Kato, T., and Kikegawa, T. (2000) In situ determination of the phase
759 boundary between wadsleyite and ringwoodite in Mg_2SiO_4. Goephysical Research
760 Letters, 27, 803–806.
761 Tange, Y., Nishihara, Y., and Tsuchiya, T. (2009) Unified analyses for *P–V–T* equation
762 of state of MgO: A solution for pressure-scale problems in high *P–T* experiments.
763 Journal of Geophysical Research, 114, B03208.
764 Trots, D.M, Kurnosov, A., Boffa Ballaran, T., and Frost, D.J. (2012) High-temperature
765 structural behaviors of anhydrous wadsleyite and forsterite. American Mineralogist,
766 97, 1582–1590.
767 Tsuchiya, T. (2003) First-principles prediction of the *P–V–T* equation of state of gold
768 and the 660-km discontinuity in Earth's mantle. Journal of Geophysical Research,
769 108, B10, 2462.
770 Wang, F., Tange, Y., Irifune, T., and Funakoshi, K. (2012) *P–V–T* equation of state of
771 stishovite up to mid-lower mantle conditions. Journal of Geophysical Research, 117,
772 B06209.
773 Watanabe, H. (1982) Thermochemical properties of synthetic high-pressure compounds
774 relevant to the Earth's mantle. In: S. Akimoto and M.H. Manghnani, Eds.,
775 High-pressure research in geophysics, p. 441−464. Center for Academic Publications,

776 Japan, Tokyo.

777 Williams, Q. and Revenaugh, J. (2005) Ancient subduction, mantle eclogite, and the 300
778 km seismic discontinuity. Geology, 33, 1–4.

779 Woodland, A.B. (1998) The orthorhombic to high-P monoclinic phase transition in
780 Mg-Fe pyroxenes: Can it produce a seismic discontinuity?. Geophysical Research
781 Letters, 25, 1241–1244.

782 Yamamoto, S., Komiya, T., Hirose, K., and Maruyama, S. (2009) Coesite and
783 clinopyroxene exsolution lamellae in chromitites: In-situ ultrahigh-pressure evidence
784 from podiform chromitites in the Luobusa ophiolite, southern Tibet. Lithos, 109,
785 314−322.

786 Yong, D., Dachs, E., Withers, A.C., and Essene, E.J. (2006) Heat capacity and phase
787 equilibria of hollandite polymorph of $KAlSi_3O_8$. Physics and Chemistry of Minerals,
788 33, 167–177.

789 Zhang, J., Li, B., Utsumi, W., and Liebermann, R.C. (1996) In situ X-ray observations
790 of the coesite–stishovite transition: reversed phase boundary and kinetics. Physics
791 and Chemistry of Minerals, 23, 1–10.

792

793 Figure captions

794

795 Figure 1. The results of high-pressure high-temperature experiments. Open, red solid,
796 gray solid and light blue solid triangles indicate that the recovered samples are
797 forsterite (Fo) + periclase (Per), anhydrous phase B (Anh-B), wadsleyite (Wd) + Per
798 and ringwoodite (Rw) + Per, respectively. Reverse triangles represent reverse runs.
799 Half red-half open triangles, half gray-half red triangles and the half light blue-half
800 gray triangle show mixtures of Anh-B + Fo + Per, Anh-B + Wd + Per and Rw + Wd
801 + Per, respectively. Solid lines are the phase boundaries of Fo + Per = Anh-B and
802 Anh-B = Wd + Per determined using the least-squares method. Dashed lines show
803 their uncertainty. The dash-dotted line is the Wd–Rw phase boundary of Inoue et al.
804 (2006) rescaled using Tsuchiya's (2003) equation of state of Au.

805 Figure 2. Temperature dependences of the lattice parameters and volume of anhydrous
806 phase B. The open circles and plus symbols are lattice parameters and volumes
807 measured in the heating and cooling processes, respectively. Red solid lines show
808 fitted curves by the least-squares method.

809 Figure 3. Thermal expansivity of anhydrous phase B. The red thick broken line
810 represents thermal expansivity determined by the high-temperature X-ray diffraction

(HTXRD) method. The solid curves were calculated using thermal Grüneisen parameters (γ_{th}) of 1.1, 1.2 and 1.3. The dash-dotted line shows a curve previously predicted by the *ab initio* calculations of Ottonello et al. (2010).

Figure 4. Measured isobaric heat capacity of anhydrous phase B. Red and blue open circles show the data obtained by the thermal relaxation method and differential scanning calorimetry, respectively. Insets show the results of the least-squares fitting individually performed in the temperature ranges of 0–20, 20–70, 70–200 and 200–380 K. The fitted curves are represented by solid lines.

Figure 5. Information on the lattice vibration of anhydrous phase B. (a) Observed Raman spectrum of anhydrous phase B. Vertical bars below the Raman spectrum indicate lattice vibrational mode frequencies for the Raman active modes (upper ones) and infra-red (IR) active and silent modes (lower ones) calculated by Ottonello et al. (2010). (b) Vibrational density of state model used for the Kieffer model calculation. Three vertical lines around 100 cm^{-1} indicate cut off frequencies of Debye-like oscillators for acoustic modes. The distribution of the optic modes based on the data shown in (a) is modeled using four rectangles (i.e., optic continua). Numbers in or above the rectangles indicate the fraction of optic modes assigned to each optic continuum.

Figure 6. Comparison of observed and calculated heat capacities for anhydrous phase B. Open circles are the isobaric heat capacity data observed in this study. Red and blue curves indicate isobaric and isochoric heat capacities calculated using the Kieffer model. The dashed line is the isobaric heat capacity obtained using *ab initio* calculations by Ottonello et al. (2010).

Figure 7. Heat capacities of Mg_2SiO_4 wadsleyite calculated using the Kieffer model. Red and blue open circles and blue diamonds are the isobaric heat capacity data measured by Akaogi et al. (2007), Ashida et al. (1987) and Watanabe (1982), respectively. Solid curves show isochoric and isobaric heat capacities obtained by the Kieffer model calculation using a vibrational density of state model which well reproduces the data of Akaogi et al. (2007).

Figure 8. Thermal expansivity of Mg_2SiO_4 wadsleyite. The solid curve shows a calculated thermal expansivity using the Grüneisen relation equation. Open squares and open triangles are the data determined experimentally by Suzuki et al. (1980) and Trots et al. (2012), respectively.

Figure 9. Forsteirte (Fo)–wadsleyite (Wd) and Wd–ringwoodite (Rw) phase boundaries in Mg_2SiO_4. Solid curves are phase equilibrium boundaries calculated thermodynamically in this study. Error bars indicate uncertainties in the calculated

boundaries caused by the errors in the phase transition enthalpies. The dash-dotted line is the Fo–Wd phase boundary determined by the high-pressure in situ experiment by Morishima et al. (1994) and the dotted and broken lines are the Wd–Rw phase boundaries determined by the high-pressure in situ experiments by Suzuki et al. (2000) and Inoue et al. (2006), respectively. Note that the boundary of Inoue et al. (2006) was recalibrated using the equation of state of Au by Tsuchiya (2003).

Figure 10. Thermodynamically calculated phase boundaries for (a) 5 Mg_2SiO_4 forsterite (Fo) + 4 MgO periclase (Per) = $Mg_{14}Si_5O_{24}$ anhydrous phase B (Anh-B) and (b) Anh-B = 5 Mg_2SiO_4 wadsleyite (Wd) + 4 Per. Solid curves indicate thermodynamically calculated boundaries under the assumption of different drop-solution enthalpies ($\Delta H_{d\text{-}s}$) for Anh-B. Broken and dash-dotted lines are the boundaries for 5 Fo + 4 Per = Anh-B determined by the high-pressure experiment of Ganguly and Frost (2006) and calculations of Ottonello et al. (2010), respectively. The dotted line is a Wd–ringwoodite (Rw) boundary determined by the high-pressure in situ experiment of Inoue et al. (2006), rescaled with Tsuchiya's (2003) equation of state of Au. Triangles represent the results of the present high-pressure experiments. Open, red solid, gray solid and light blue solid triangles indicate the phases of Fo + Per, Anh-B, Wd + Per and Rw + Per, respectively. Reverse triangles represent reverse

runs. Half red-half open triangles, half gray-half red triangles and the half light blue-half gray triangle show phase assemblies of Anh-B + Fo + Per, Anh-B + Wd + Per and Rw + Wd + Per, respectively.

Figure 11. Thermodynamically calculated phase relations in $Mg_{14}Si_5O_{24}$. Anh-B: anhydrous phase B; Fo: forsterite; Wd: wadsleyite; Rw: ringwoodite; Per: periclase. In this calculation, the optimized formation enthalpy from elements for Anh-B of –13208 kJ/mol was adopted. Obtained phase equilibrium boundaries are shown by solid curves. The star symbol indicates the run condition (16.5 GPa and 2623 K) of a melting experiment of Fo performed by Presnall and Gasparik (1990), in which coexistence of Anh-B with liquid was observed.

Figure 12. Thermodynamically calculated phase relations in Mg_2SiO_4. Solid lines are calculated equilibrium boundaries. Anh-B: $Mg_{14}Si_5O_{24}$ anhydrous phase B; St: SiO_2 stishovite; Fo: Mg_2SiO_4 forsterite; Wd: Mg_2SiO_4 wadsleyite; Rw: Mg_2SiO_4 ringwoodite. The area surrounded by broken lines is the stability field of Anh-B + St calculated by assuming the formation enthalpy from elements ($\Delta_f H^o_{298}$) for Anh-B of –13236 kJ/mol. If a value of $\Delta_f H^o_{298}$ (Anh-B) negatively smaller than –13235 kJ/mol is adopted, the stability field of Anh-B + St never appears.

Table 1. Results of high-pressure high-temperature experiments

Run no.	Starting material	*P* (GPa)	*T* (K)	Time (h)	Recovered phases
25	Fo + Per	12	1673	3	Fo, Per
24	Fo + Per	13	1673	3	Anh-B, Fo, Per
9	Fo + Per	17	1673	3	Anh-B
10	Fo + Per	18	1673	3	Anh-B
12	Fo + Per	19	1673	3	Wd, Per
21	Fo + Per	12	1873	3	Fo, Per
27	Anh-B	12	1873	3	Anh-B, Fo, Per
22	Fo + Per	13	1873	3	Fo, Per, Anh-B
23	Fo + Per	13.5	1873	3	Anh-B, Fo, Per
26	Fo + Per	15	1873	3	Anh-B
6	Fo + Per	18	1873	1	Anh-B >> Wd, Per
8	Fo + Per	18	1873	2.5	Anh-B >> Wd, Per
17	Wd + Per	18.5	1873	3	Wd, Per, Anh-B
5	Fo + Per	19	1873	3	Wd, Per
11	Fo + Per	19.3	1873	3	Wd, Per >> Anh-B
4	Fo + Per	19	1873	3	Wd, Per
2	Fo + Per	20	1873	3	Wd, Rw, Per
1	Fo + Per	22	1873	3	Rw, Per
19	Fo + Per	12.5	2073	3	Fo, Per
28	Anh-B	12.5	2073	3	Anh-B, Fo, Per
20	Fo + Per	13.5	2073	3	Anh-B >> Fo, Per
14	Fo + Per	18	2073	3	Anh-B
16	Fo + Per	19	2073	2.5	Anh-B >> Wd, Per
18	Wd + Per	19.3	2073	3	Wd, Per, Anh-B
15	Fo + Per	19.5	2073	1.5	Wd, Per >> Anh-B
3	Fo + Per	20	2073	2.5	Wd, Per

Table 2. Lattice parameters and unit cell volumes of anhydrous phase B measured by high-temperature powder X-ray diffraction method at ambient pressure

T (K)	*a* (Å)	*b* (Å)	*c* (Å)	*V* (Å^3)
303	5.887(6)	14.199(7)	10.081(7)	842.6(7)
373	5.890(5)	14.210(7)	10.085(7)	844.1(7)
423	5.893(6)	14.225(8)	10.089(7)	845.7(8)
473	5.896(5)	14.220(7)	10.100(7)	846.5(7)
523	5.898(5)	14.229(7)	10.102(7)	847.7(6)
573	5.902(5)	14.230(7)	10.106(7)	849.0(7)
623	5.905(5)	14.246(7)	10.111(7)	850.5(6)
673	5.909(5)	14.249(7)	10.117(7)	851.8(7)
723	5.913(5)	14.258(7)	10.121(7)	853.3(7)
773	5.915(5)	14.265(7)	10.128(7)	854.6(7)
723	5.912(5)	14.260(7)	10.122(6)	853.3(6)
673	5.910(5)	14.250(7)	10.116(6)	851.8(6)
623	5.905(5)	14.246(7)	10.111(7)	850.6(7)
573	5.902(5)	14.236(7)	10.105(6)	849.0(6)
523	5.900(5)	14.228(7)	10.101(7)	847.7(6)
473	5.895(5)	14.223(7)	10.090(7)	846.3(6)
423	5.893(5)	14.217(7)	10.088(6)	845.1(6)
373	5.890(5)	14.206(7)	10.090(7)	843.8(7)
303	5.887(5)	14.197(7)	10.077(7)	842.2(7)

Table 3. High-temperature isobaric heat capacity of $Mg_{14}Si_5O_{24}$ anhydrous phase B measured using a differential scanning calorimeter (DSC)

Section I		Section II		Section III		Section IV	
T (K)	C_P (J/mol·K)	T (K)	C_P (J/mol·K)	T (K)	C_P (J/mol·K)	T (K)	C_P (J/mol·K)
302.5	738(2)	382.5	845(3)	462.5	908(5)	540.0	956(13)
307.5	750(4)	387.5	850(3)	467.5	915(6)	560.0	966(11)
312.5	754(1)	392.5	854(4)	472.5	917(6)	580.0	976(14)
317.5	765(4)	397.5	859(4)	477.5	922(6)	600.0	983(13)
322.5	771(6)	402.5	863(4)	482.5	925(6)	620.0	991(14)
327.5	780(4)	407.5	868(5)	487.5	928(6)	640.0	999(15)
332.5	786(4)	412.5	871(5)	492.5	931(6)	660.0	1007(16)
337.5	793(3)	417.5	876(5)	497.5	935(6)	680.0	1013(15)
342.5	799(2)	422.5	881(5)	502.5	938(8)	700.0	1019(15)
347.5	806(2)	427.5	884(5)	507.5	942(6)	720.0	1025(16)
352.5	812(4)	432.5	888(5)	512.5	945(7)	740.0	1031(17)
357.5	818(3)	437.5	892(4)	517.5	947(6)	760.0	1036(17)
362.5	824(4)	442.5	896(5)	522.5	951(7)		
367.5	831(3)	447.5	901(7)	527.5	953(7)		
372.5	835(3)	452.5	904(4)	532.5	956(8)		
377.5	842(4)	457.5	906(4)	537.5	959(7)		
382.5	847(4)	462.5	909(4)	542.5	962(7)		
387.5	851(7)	467.5	916(5)	547.5	964(7)		
392.5	855(5)	472.5	920(5)	552.5	967(6)		
397.5	860(4)	477.5	924(5)	557.5	970(7)		

Numbers in parentheses are uncertainties in last significant figure, which were obtained from twice the standard deviation of the mean.

954 Table 4. Low-temperature isobaric heat capacity of $Mg_{14}Si_5O_{24}$ anhydrous phase B
955 measured using a Physical Property Measurement System (PPMS)

T (K)	C_P (J/mol·K)	T (K)	C_P (J/mol·K)	T (K)	C_P (J/mol·K)
2.0	0.00603(8)	105.1	190.0(4)	206.9	536.8(6)
3.9	0.0127(2)	107.1	197.5(4)	208.9	543.3(6)
5.9	0.0329(5)	109.1	205.5(5)	210.8	547.7(8)
8.1	0.080(2)	111.1	212.6(5)	212.8	554.1(8)
10.1	0.151(2)	113.1	220.7(5)	214.8	556.9(10)
12.1	0.250(5)	115.1	227.8(5)	216.8	559.7(5)
14.1	0.404(6)	117.0	235.3(5)	218.8	564.7(6)
15.9	0.588(9)	119.0	243.1(5)	220.8	570.8(6)
17.9	0.843(9)	121.0	249.8(5)	222.8	576.2(7)
20.0	1.14(2)	123.0	257.3(5)	224.8	583.0(10)
22.0	1.56(2)	125.0	264.8(5)	226.8	586.5(11)
24.0	2.07(3)	127.0	272.4(5)	228.8	589.6(6)
26.0	2.70(3)	129.0	280.4(5)	230.8	595.9(9)
28.1	3.51(3)	131.0	287.4(4)	232.8	599.8(9)
30.2	4.52(3)	133.0	295.2(3)	234.8	602.0(9)
32.2	5.67(4)	135.0	303.3(3)	236.8	610.3(10)
34.3	7.02(5)	137.0	310.5(3)	238.8	608.8(9)
36.3	8.71(7)	139.0	317.4(4)	240.8	614.7(13)
38.4	10.59(6)	141.0	325.8(3)	242.8	623.5(11)
40.5	12.73(6)	143.0	332.3(3)	244.8	628.6(9)
42.5	15.25(11)	145.0	339.9(4)	246.8	636.7(9)
44.6	17.58(8)	147.0	346.0(3)	248.8	642.3(18)
46.7	20.46(9)	148.9	353.0(5)	250.8	641.3(12)
48.7	23.52(9)	150.9	360.6(4)	252.8	648.9(8)
50.8	26.91(9)	152.9	367.7(5)	254.7	650.9(11)
52.8	30.53(10)	154.9	373.0(3)	256.7	658.2(10)
54.8	34.2(2)	156.9	380.2(4)	258.7	655.6(15)
56.8	38.4(2)	158.9	388.4(5)	260.7	664.7(11)
58.9	42.8(2)	160.9	395.1(4)	262.7	664.0(12)
60.9	47.6(2)	162.9	401.1(4)	264.7	667.4(15)
63.0	52.4(2)	164.9	408.7(3)	266.7	666.5(18)
65.0	57.9(2)	166.9	417.1(4)	268.7	681.1(17)
67.0	63.3(2)	168.9	423.0(3)	270.7	680.4(16)

69.0	68.8(2)	170.9	429.0(3)	272.7	682.5(17)
71.0	74.5(3)	172.9	436.2(3)	274.7	688.3(15)
73.0	80.4(2)	174.9	440.3(4)	276.7	693.5(15)
74.9	86.1(3)	176.9	445.9(3)	278.7	699.7(15)
77.0	92.0(3)	178.9	453.2(3)	280.7	702.1(15)
79.0	98.0(2)	180.9	461.9(6)	282.7	706.5(19)
80.9	105.3(4)	182.9	467.6(4)	284.7	704.9(24)
82.9	110.5(3)	184.9	472.3(4)	286.7	711.2(24)
85.0	117.2(2)	186.9	476.1(4)	288.7	712.0(21)
87.0	124.2(3)	188.9	484.2(4)	290.7	711.8(20)
89.0	131.1(3)	190.9	490.3(5)	292.7	719.4(24)
91.0	138.1(4)	192.9	497.7(7)	294.7	717.6(26)
93.0	145.2(4)	194.9	502.6(8)	296.7	725.0(24)
95.0	152.5(4)	196.9	510.2(5)	298.7	726.8(27)
97.0	160.0(4)	198.9	514.3(4)	300.7	734.8(28)
99.1	167.3(4)	200.9	520.4(5)	302.6	734.2(25)
101.1	175.0(4)	202.9	526.3(5)		
103.1	182.6(4)	204.8	531.8(6)		

Numbers in parentheses are uncertainties in last significant figure.

This is a preprint, the final version is subject to change, of the American Mineralogist (MSA)
Cite as Authors (Year) Title. American Mineralogist, in press.
(DOI will not work until issue is live.) DOI: http://dx.doi.org/10.2138/am-2017-6115

963 Table 5. Coefficients for fitted C_P equations
964 of anhydrous phase B in a low temperature
965 region

	Coefficient
T: 0–20 K	
k_6	$(1.4543\pm0.0060)\times10^{-4}$
χ^2	1.274
R^2	0.99929
T: 20–70 K	
k_0	$(2.4036\pm0.0917)\times10$
k_2	$(-1.9128\pm0.1782)\times10^{3}$
k_4	-1.5349 ± 0.0307
k_5	$(3.1674\pm0.0266)\times10^{-2}$
χ^2	3.404
R^2	0.99995
T: 70–200 K	
k_0	$(1.5708\pm 0.6587)\times10^{3}$
k_1	$(-1.9024\pm0.6096)\times10^{4}$
k_2	$(5.3763\pm1.4376)\times10^{6}$
k_3	$(-1.3569\pm0.3742)\times10^{8}$
k_4	1.1361 ± 1.8168
k_5	$(-1.3137\pm2.612)\times10^{-3}$
χ^2	3.331
R^2	0.99997
T: 200–380 K	
k_0	$(1.4964\pm0.098)\times10^{3}$
k_1	$(-1.0859\pm0.2570)\times10^{4}$
k_2	$(-1.9386\pm0.6796)\times10^{7}$
k_3	$(2.1885\pm0.6927)\times10^{9}$
χ^2	4.754
R^2	0.99935

966 $C_P\,(T) = k_0 + k_1T^{-0.5} + k_2T^{-2} + k_3T^{-3} + k_4T +$
967 $k_5T^2 + k_6T^3$.

968 $\chi^2 = \left[\sum_i^n \frac{(Cp_i - Cp(T_i))^2}{\sigma_i^2}\right]/(n-m)$ where n is
969 the number of data and m is the number of
970 fitted parameters.
971 $R^2 = 1 - \frac{\sum(Cp_i - Cp(T_i))^2}{\sum(Cp_i - \langle Cp\rangle)^2}$ where $\langle Cp\rangle$ is the
972 mean value of C_{Pi}.
973
974

975 Table 6. Observed Raman peaks of
976 anhydrous phase B

No.	Raman shift (cm^{-1})	No.	Raman shift (cm^{-1})
1	125	19	464
2	164	20	475
3	170	21	481
4	195	22	511
5	216	23	520
6	238	24	559
7	250	25	570
8	309	26	590
9	332	27	601
10	345	28	643
11	360	29	683
12	371	30	819
13	389	31	842
14	405	32	871
15	415	33	894
16	437	34	904
17	447	35	949
18	460	36	1022

977
978
979

Table 7. Lattice vibrational density of states models for $Mg_{14}Si_5O_{24}$ anhydrous phase B and Mg_2SiO_4 wadsleyite

Type	Lower limit (cm^{-1})	Upper limit (cm^{-1})	Number of modes
$Mg_{14}Si_5O_{24}$ Anh-B			
D (TA-1)	0	67	1
D (TA-2)	0	93	1
D (LA)	0	128	1
OC-1	187	540	190
OC-2	540	700	33
OC-3	790	910	26
OC-4	950	1050	6
Mg_2SiO_4 Wd			
D (TA-1)	0	108	1
D (TA-2)	0	122	1
D (LA)	0	199	1
OC-1	185	630	68
OC-2	800	1000	10
E	–	700	3

D: Debye oscillator; OC: optic continuum; E: Einstein oscillator.
TA: transverse acoustic mode; LA: longitudinal acoustic mode.

This is a preprint, the final version is subject to change, of the American Mineralogist (MSA)
Cite as Authors (Year) Title. American Mineralogist, in press.
(DOI will not work until issue is live.) DOI: http://dx.doi.org/10.2138/am-2017-6115

Table 8. Results of heat capacity and thermal expansivity calculations for $Mg_{14}Si_5O_{24}$ anhydrous phase B and Mg_2SiO_4 wadsleyite

	$Mg_{14}Si_5O_{24}$ Anh-B			**Mg_2SiO_4 Wd**		
T (K)	C_V (J/mol·K)	$\alpha\times10^5$ (1/K)	C_P (J/mol·K)	C_V (J/mol·K)	$\alpha\times10^5$ (1/K)	C_P (J/mol·K)
10	0.19	0.00056	0.19	0.02	0.00040	0.02
20	1.78	0.0053	1.78	0.26	0.0047	0.26
30	4.75	0.014	4.75	1.01	0.018	1.01
40	10.75	0.032	10.75	2.43	0.043	2.43
50	22.74	0.068	22.74	4.74	0.084	4.74
60	41.85	0.126	41.86	8.01	0.143	8.01
70	67.49	0.203	67.50	12.14	0.217	12.14
80	98.31	0.297	98.34	16.95	0.304	16.95
90	132.86	0.402	132.92	22.25	0.399	22.26
100	169.80	0.514	169.90	27.89	0.501	27.90
150	358.76	1.096	359.46	57.00	1.031	57.12
200	518.19	1.597	520.17	82.32	1.498	82.64
250	639.49	1.988	643.30	102.03	1.870	102.65
300	729.71	2.289	735.47	116.89	2.155	117.85
400	847.56	2.708	859.05	136.53	2.552	138.39
500	916.21	2.982	933.04	148.07	2.807	150.82
600	958.60	3.180	980.72	155.23	2.984	158.87
700	986.24	3.336	1013.80	159.91	3.119	164.46
800	1005.11	3.468	1038.38	163.12	3.228	168.61
900	1018.50	3.586	1057.83	165.39	3.321	171.86
1000	1028.32	3.695	1074.09	167.06	3.405	174.54
1100	1035.72	3.801	1088.34	168.32	3.483	176.86
1200	1041.43	3.905	1101.31	169.29	3.558	178.92
1300	1045.91	4.009	1113.49	170.06	3.630	180.83
1400	1049.51	4.114	1125.20	170.67	3.702	182.62
1500	1052.42	4.221	1136.65	171.17	3.773	184.33
1600	1054.82	4.332	1148.00	171.57	3.845	186.00
1700	1056.82	4.445	1159.33	171.92	3.917	187.64
1800	1058.50	4.564	1170.72	172.20	3.991	189.27
1900	1059.93	4.687	1182.20	172.44	4.066	190.89
2000	1061.15	4.816	1193.81	172.65	4.143	192.51

2100	1062.21	4.951	1205.54	172.83	4.222	194.13
2200	1063.12	5.092	1217.40	172.99	4.304	195.77
2300	1063.92	5.241	1229.36	173.13	4.388	197.41
2400	1064.63	5.399	1241.41	173.25	4.475	199.07
2500	1065.25	5.566	1253.50	173.35	4.565	200.74

1006

1007

Table 9. Thermochemical and thermoelastic parameters used for thermodynamic calculations

	Anh-B	Fo	Wd	Rw	Per	St
$\Delta_f H^o_{298}$ (kJ/mol)	–132108 [a]	–2174.0 [a]	–2148.0 [a]	–2134.8 [a]	–601.6 [b]	–874.7 [a]
S^o_{298} (J/mol·K)	544.4 [a]	94.1 [b]	86.4 [c]	82.7 [c]	26.9 [b]	24.0 [d]
EoS	HTBM	HTBM	HTBM	HTBM	MGD-BM	MGD-V
V_0(298) (cm^3/mol)	252.61 [a]	43.66 [e]	40.53 [f]	39.49 [g]	11.25 [h]	14.01 [i]
K_T(298) (GPa)	151.5 [j]	128.75 [k]	174 [l]	184 [m]	160.64 [h]	292 [n]
K_T'	5.5 [j]	4.6 [k]	4.3 [l]	4.8 [m]	4.22 [h]	5.01 [n]
$(\partial K_T/\partial T)_P$ (GPa/K)	–0.0275 [a]	–0.0234 [k]	–0.0237 [a]	–0.019 [m]	—	—
γ_0	—	—	—	—	1.431 [h]	1.67 [n]
θ_{D0} (K)	—	—	—	—	761 [h]	1130 [n]
k	—	—	—	—	0.290 [h]	1 [n]
q	—	—	—	—	3.5 [h]	3 [n]
$\alpha(T) = a_0 + a_1T + a_2T^{-1} + a_3T^{-2}$ (1/K)						
$a_0\times10^5$	1.990 [a]	2.384 [o]	2.682 [a]	2.479 [m]	—	—
$a_1\times10^9$	13.21	12.28	7.327	3.951	—	—
$a_2\times10^4$	52.01	29.80	6.331	–2.271	—	—
$a_3\times10$	–16.91	–9.309	–8.841	–5.604	—	—
$C_P(T) = c_0 + c_1T + c_2T^{-0.5} + c_3T^{-1} + c_4T^{-2} + c_5T^{-3}$ (J/mol·K)						
c_0	300.5 [a]	175.7 [k]	79.66 [a]	121.9 [m]	–46.25 [m]	85.78 [p]
$c_1\times10^2$	17.91	1.580	2.314	1.358	1.452	0
$c_2\times10^{-3}$	37.02	0	4.749	2.725	5.207	–0.3455
$c_3\times10^{-5}$	–5.942	–0.1574	–0.7996	–0.4703	–0.9168	0
$c_4\times10^{-6}$	17.11	–1.192	1.259	–2.965	10.51	–3.605
$c_5\times10^{-8}$	9.302	1.317	2.589	5.944	–8.765	4.511

Anh-B: $Mg_{14}Si_5O_{24}$ anhydrous phase B; Fo: Mg_2SiO_4 forsterite; Wd: Mg_2SiO_4 wadsleyite; Rw: Mg_2SiO_4 ringwoodite; Per: MgO periclase; St: SiO_2 stishovite.

HTBM: third order high-temperature Birch−Murnaghan equation of state.

MGD-BM: Mie−Grüneisen−Debye equation of state with a third order Birch−Murnaghan equation of state at 298 K.

MGD-V: Mie−Grüneisen−Debye equation of state with a Vinet equation of state at 298

K.

[a] This study.

[b] Robie and Hemingway (1995).

[c] Akaogi et al. (2007).

[d] Akaogi et al. (2011).

[e] Lager et al. (1981).

[f] Finger et al. (1993).

[g] Sasaki et al. (1982).

[h] Tange et al. (2009).

[i] Nishihara et al. (2005).

[j] Crichton et al. (1999).

[k] Optimized by Jacobs and Oonk (2001) using α of Kajiyoshi (1986).

[l] Fei et al. (1992).

[m] Kojitani et al. (2016).

[n] Wang et al. (2012).

[o] Converted from α equation optimized by Jacobs and Oonk (2001).

[p] Akaogi et al. (1995).

Table 10. Drop-solution enthalpies of Mg_2SiO_4 polymorphs and their constituent oxides in $2PbO \cdot B_2O_3$ solvent at 978 K

Phase	$\Delta H^o_{d\text{-}s}$ (kJ/mol)		Reference
Mg_2SiO_4 forsterite	169.35±1.19	[9]	Akaogi et al. (2007)
Mg_2SiO_4 forsterite	168.21±0.44	[13]	Kojitani et al. (2016)
Mg_2SiO_4 wadsleyite	142.19±1.33	[7]	Akaogi et al. (2007)
Mg_2SiO_4 ringwoodite	129.31±0.98	[7]	Akaogi et al. (2007)
Mg_2SiO_4 ringwoodite	128.75±1.00	[8]	Kojitani et al. (2016)
MgO periclase	33.74±0.50		Kojitani et al. (2012b)
SiO_2 quartz	40.05±0.18	[6]	Akaogi et al. (1995)
SiO_2 stishovite	3.04±0.46	[6]	Akaogi et al. (1995)

Errors are the standard deviation of the mean. Numerals in square brackets represent number of measurements.

This is a preprint, the final version is subject to change, of the American Mineralogist (MSA)
Cite as Authors (Year) Title. American Mineralogist, in press.
(DOI will not work until issue is live.) DOI: http://dx.doi.org/10.2138/am-2017-6115

Figure 1

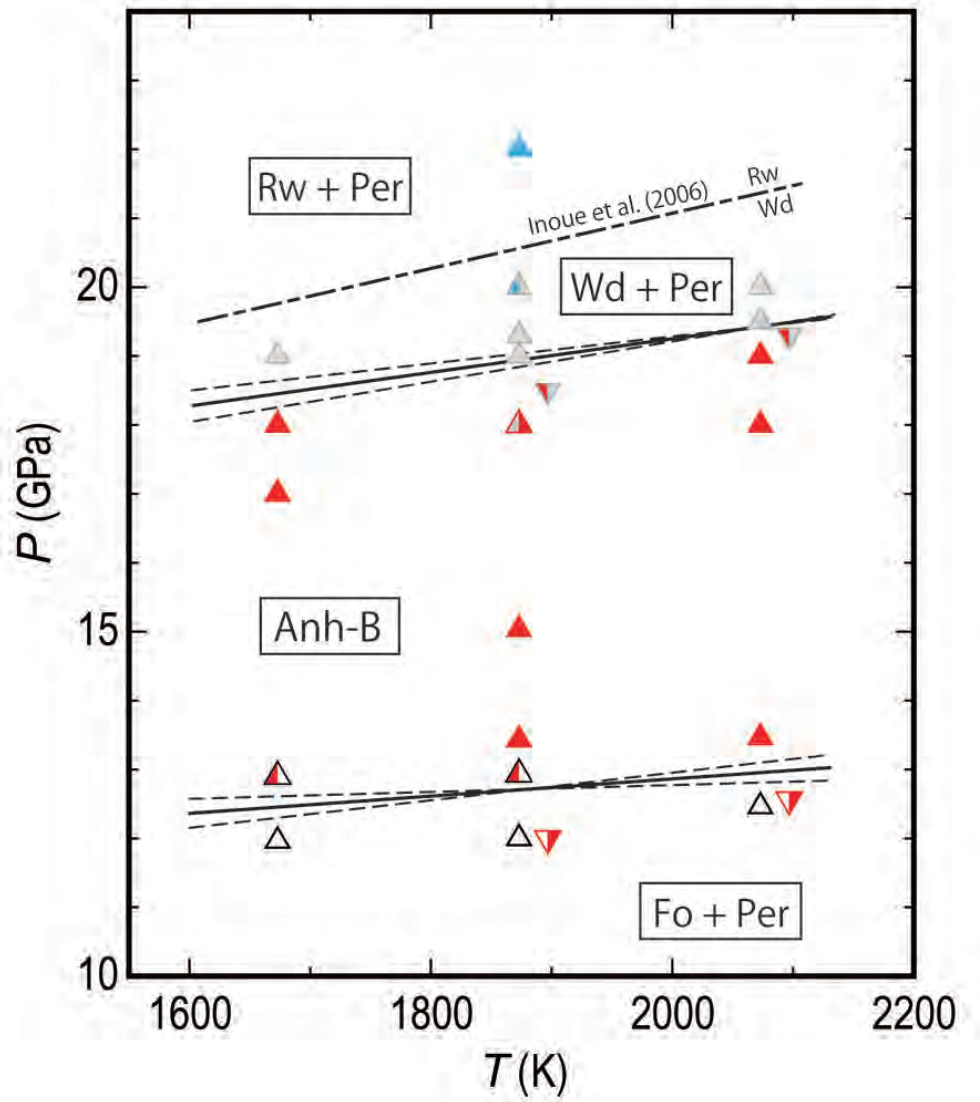

This is a preprint, the final version is subject to change, of the American Mineralogist (MSA)
Cite as Authors (Year) Title. American Mineralogist, in press.
(DOI will not work until issue is live.) DOI: http://dx.doi.org/10.2138/am-2017-6115

Figure 2

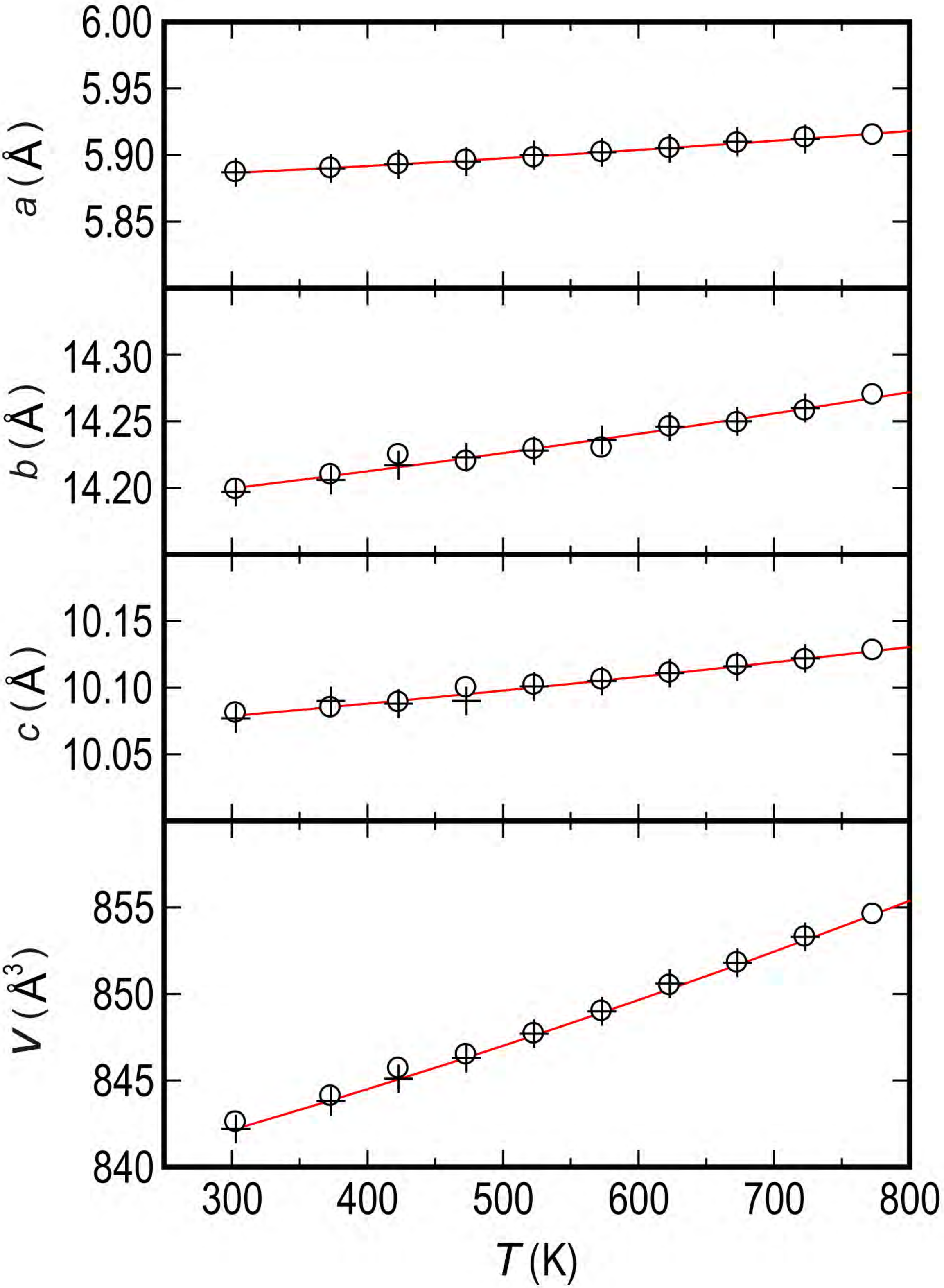

This is a preprint, the final version is subject to change, of the American Mineralogist (MSA)
Cite as Authors (Year) Title. American Mineralogist, in press.
(DOI will not work until issue is live.) DOI: http://dx.doi.org/10.2138/am-2017-6115

Figure 3

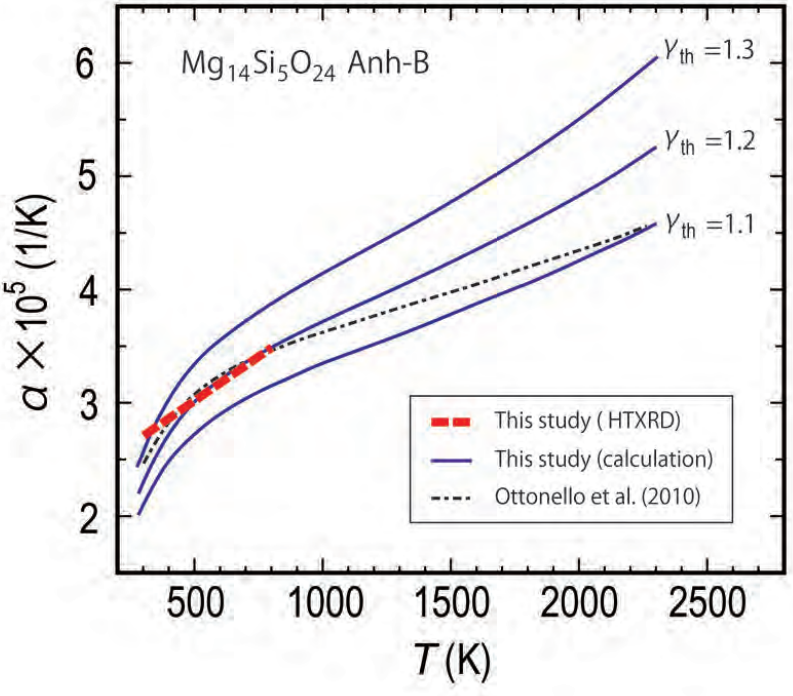

This is a preprint, the final version is subject to change, of the American Mineralogist (MSA)
Cite as Authors (Year) Title. American Mineralogist, in press.
(DOI will not work until issue is live.) DOI: http://dx.doi.org/10.2138/am-2017-6115

Figure 4

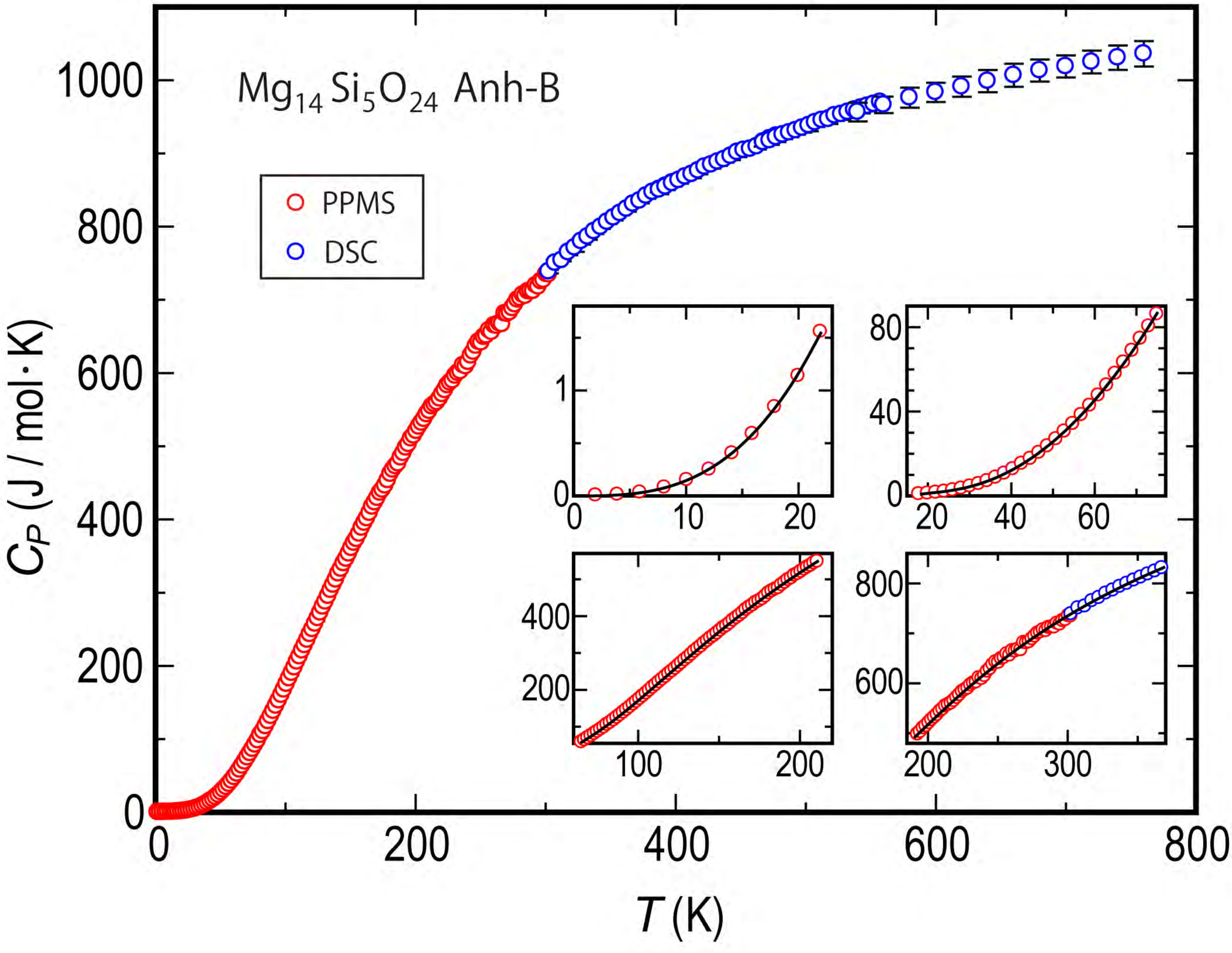

This is a preprint, the final version is subject to change, of the American Mineralogist (MSA)
Cite as Authors (Year) Title. American Mineralogist, in press.
(DOI will not work until issue is live.) DOI: http://dx.doi.org/10.2138/am-2017-6115

Figure 5

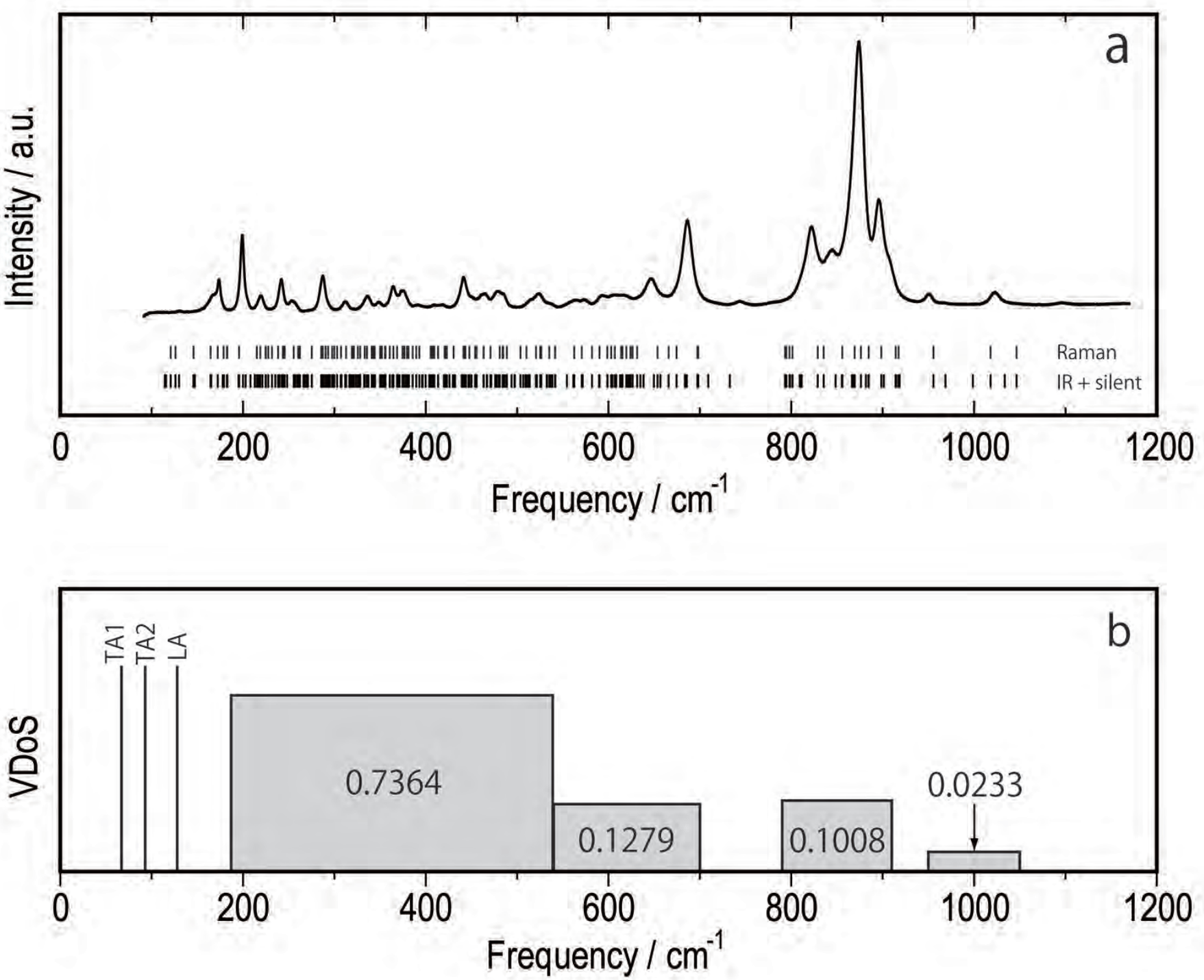

This is a preprint, the final version is subject to change, of the American Mineralogist (MSA)
Cite as Authors (Year) Title. American Mineralogist, in press.
(DOI will not work until issue is live.) DOI: http://dx.doi.org/10.2138/am-2017-6115

Figure 6

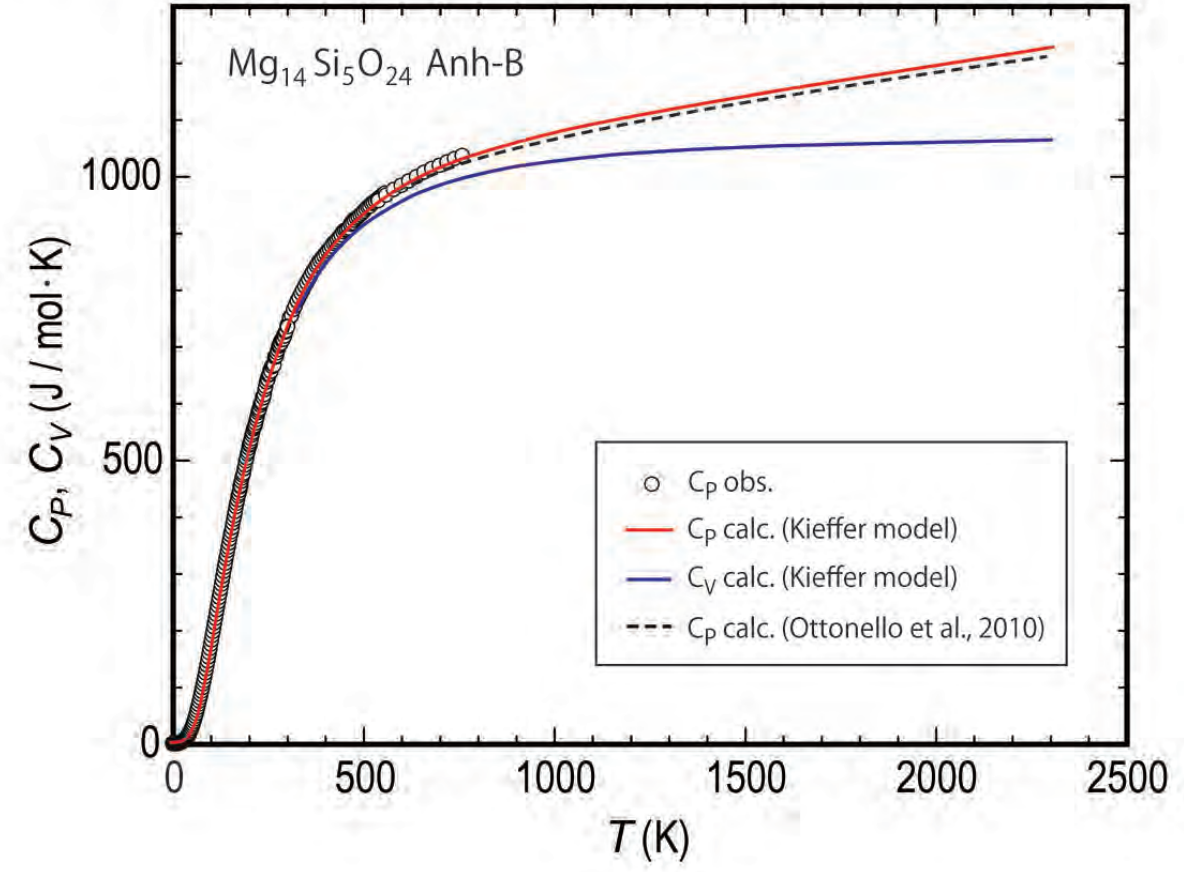

This is a preprint, the final version is subject to change, of the American Mineralogist (MSA)
Cite as Authors (Year) Title. American Mineralogist, in press.
(DOI will not work until issue is live.) DOI: http://dx.doi.org/10.2138/am-2017-6115

Figure 7

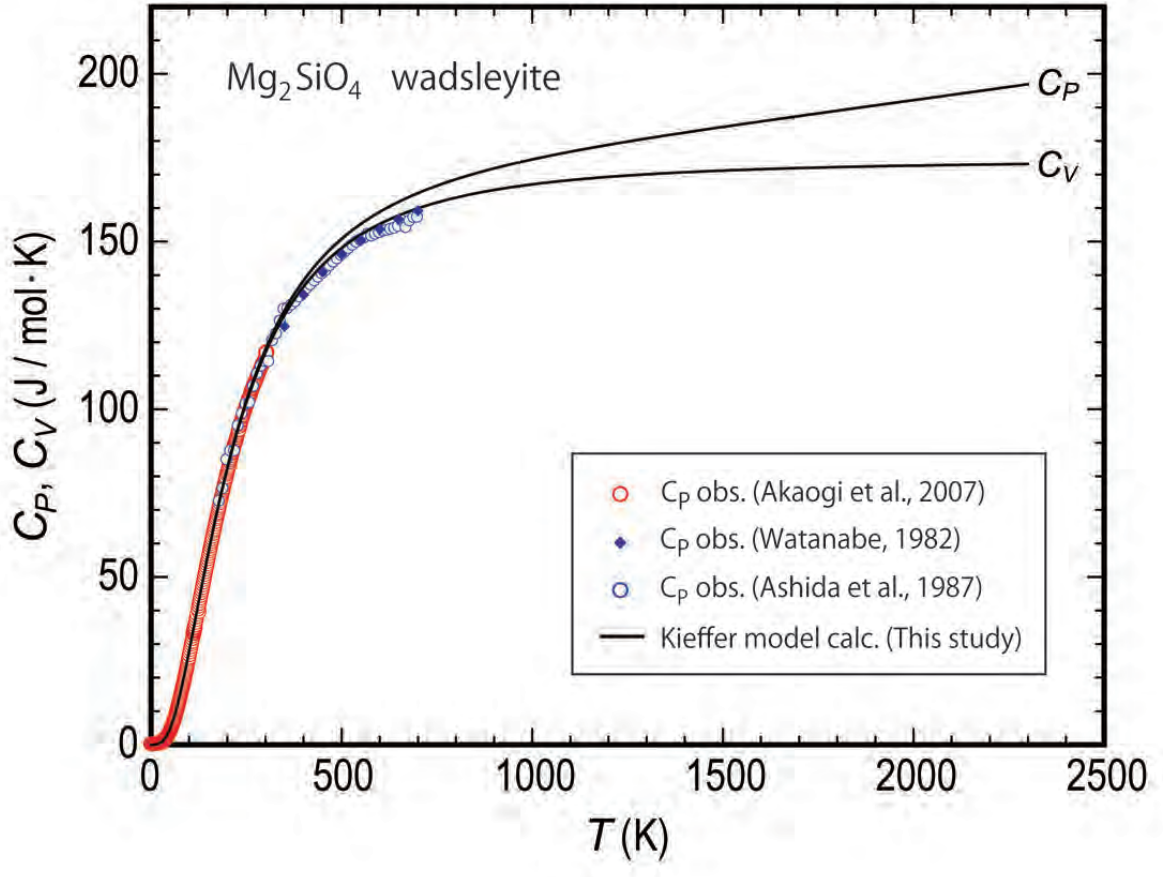

This is a preprint, the final version is subject to change, of the American Mineralogist (MSA)
Cite as Authors (Year) Title. American Mineralogist, in press.
(DOI will not work until issue is live.) DOI: http://dx.doi.org/10.2138/am-2017-6115

Figure 8

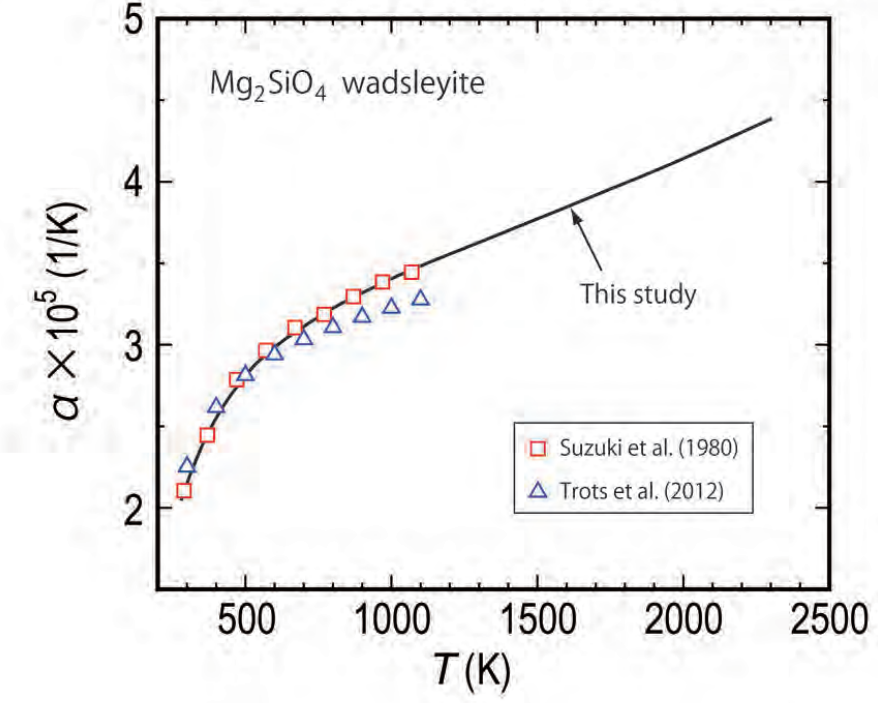

This is a preprint, the final version is subject to change, of the American Mineralogist (MSA)
Cite as Authors (Year) Title. American Mineralogist, in press.
(DOI will not work until issue is live.) DOI: http://dx.doi.org/10.2138/am-2017-6115

Figure 9

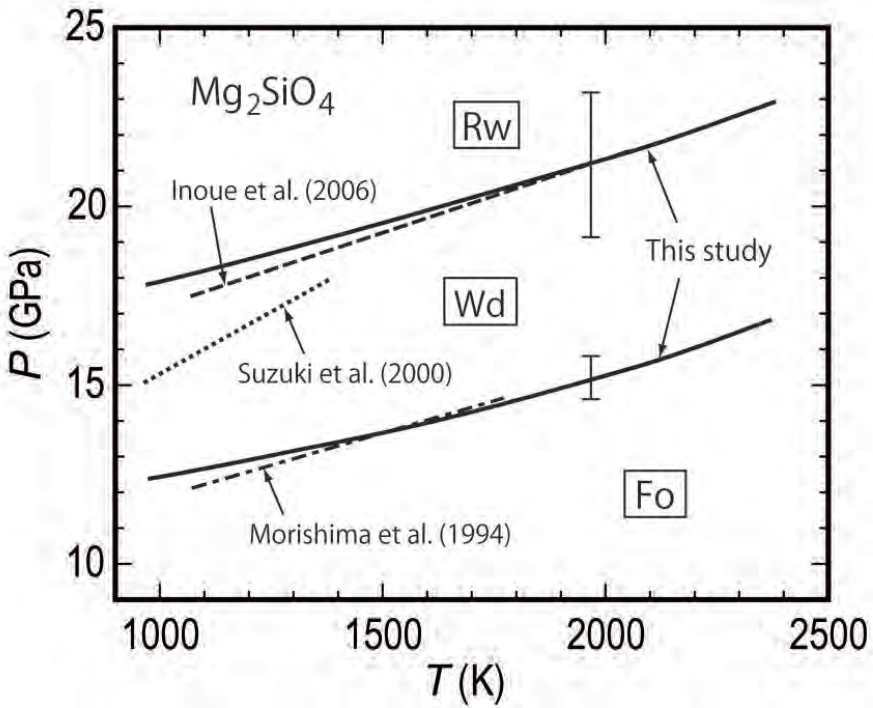

This is a preprint, the final version is subject to change, of the American Mineralogist (MSA)
Cite as Authors (Year) Title. American Mineralogist, in press.
(DOI will not work until issue is live.) DOI: http://dx.doi.org/10.2138/am-2017-6115

Figure 10

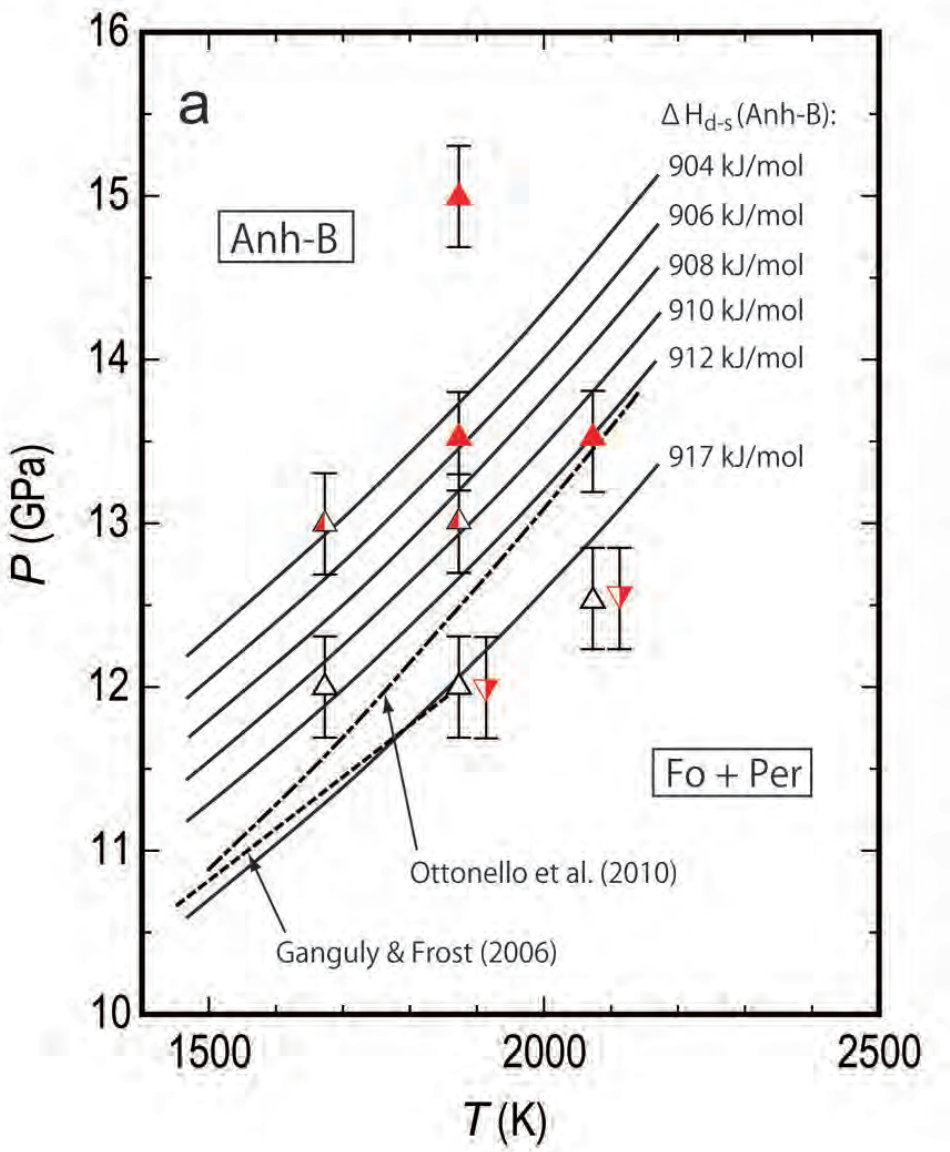

This is a preprint, the final version is subject to change, of the American Mineralogist (MSA)
Cite as Authors (Year) Title. American Mineralogist, in press.
(DOI will not work until issue is live.) DOI: http://dx.doi.org/10.2138/am-2017-6115

Figure 10

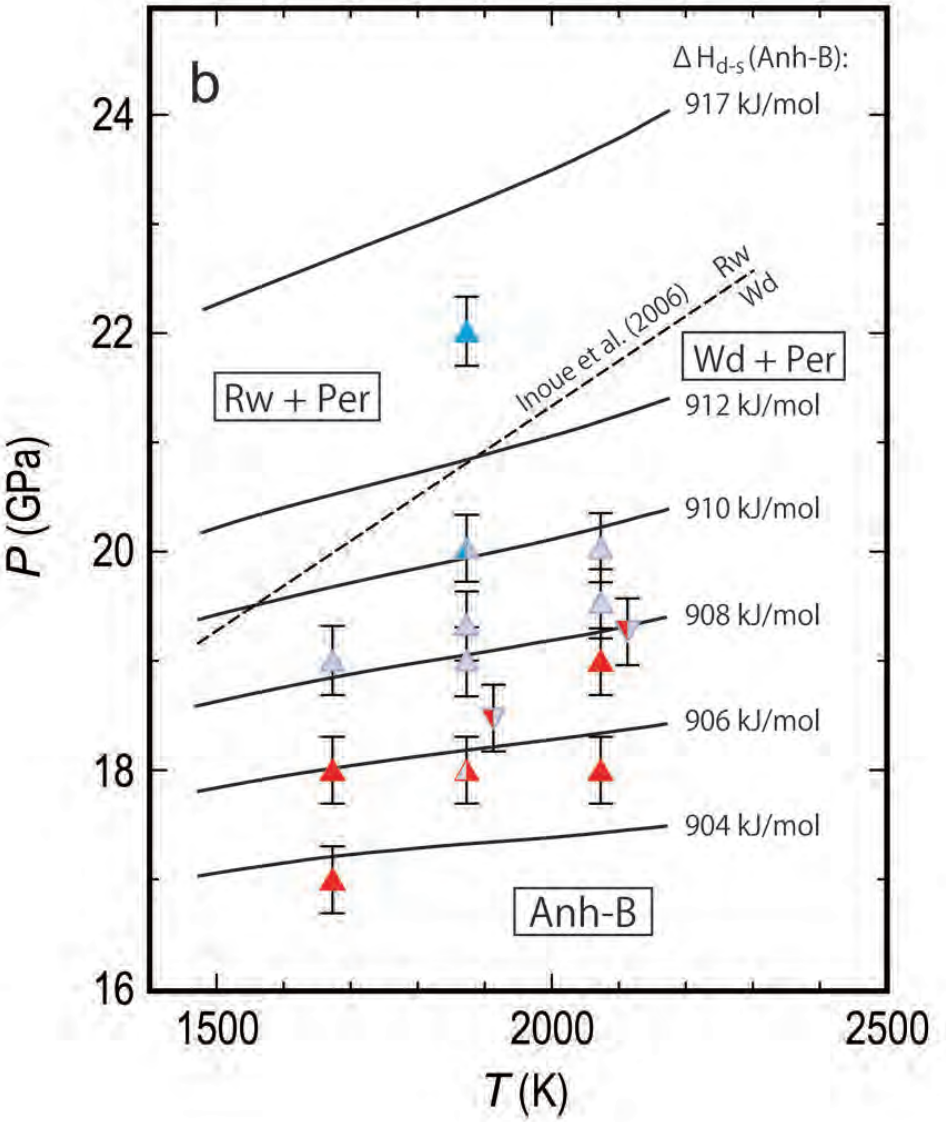

This is a preprint, the final version is subject to change, of the American Mineralogist (MSA)
Cite as Authors (Year) Title. American Mineralogist, in press.
(DOI will not work until issue is live.) DOI: http://dx.doi.org/10.2138/am-2017-6115

Figure 11

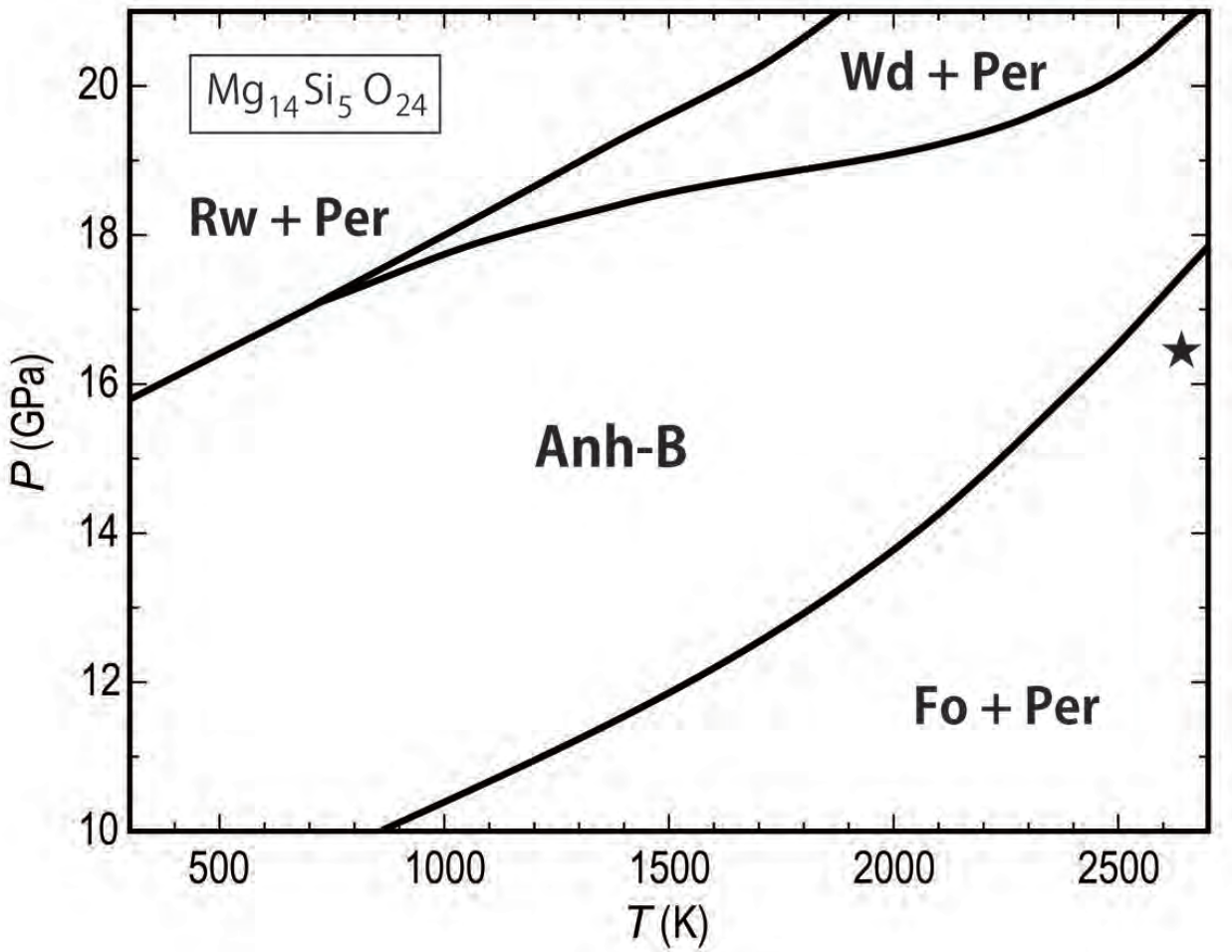

This is a preprint, the final version is subject to change, of the American Mineralogist (MSA)
Cite as Authors (Year) Title. American Mineralogist, in press.
(DOI will not work until issue is live.) DOI: http://dx.doi.org/10.2138/am-2017-6115

Figure 12